

# UNIVERSITÀ DEGLI STUDI DI PADOVA

**Dipartimento di Fisica e Astronomia "Galileo Galilei"**

**Master Degree in Physics**


**Final Dissertation**

# Search for SuperWIMPs using the data collected by the GERDA experiment


**Thesis supervisor**

**Prof. Riccardo Brugnera**

**Thesis co-supervisor**

**Dott.ssa Valentina Biancacci**

**Candidate**

**Sofia Calgaro**


**Academic Year 2020/2021**

*A Irene*

# Contents

**Introduction** **1**

**1 Search for SuperWIMPs** **3**
1.1 Dark Matter and SuperWIMPs . . . 3
1.2 Axion-Like Particles and Dark Photons . . . 4
1.3 SuperWIMP Signature . . . 4

**2 The GERDA Experiment** **7**
2.1 Design of the GERDA experiment . . . 7
2.1.1 General Layout . . . 9
2.1.2 Germanium Detectors . . . 9
2.1.3 LAr Veto System . . . 12
2.1.4 Muon Veto System . . . 12

**3 Analysis of Data Collected by GERDA** **13**
3.1 Search for SuperWIMPs at GERDA . . . 13
3.2 Analysis Procedure . . . 13
3.2.1 Physics Dataset . . . 13
3.2.2 Bayesian Analysis . . . 15
3.2.3 Fit Model . . . 16
3.2.4 Fit Parameters . . . 18
3.3 Detection Efficiency . . . 20
3.3.1 Electron Detection Efficiency . . . 21

**4 Analysis Results** **23**
4.1 Signal Counting Rate Limits . . . 23
4.2 Monte Carlo Study of the Analysis Procedure . . . 26
4.3 SuperWIMP Coupling Strengths . . . 27

**Summary and Conclusions** **31**

**Appendix A** **33**

**Appendix B** **35**

**List of Acronyms** **37**

**Bibliography** **39**

# Introduction

Evidence for Dark Matter (DM) in our Universe has been found in many different contexts. Over the last decades, various signatures were observed for a wide range of astrophysical and cosmological systems.

Despite these observations, many questions still need to be answered, especially regarding the nature of DM. For this reason, new theories are continuously being proposed together with the help of experimental results coming from different detecting techniques, like direct searches, indirect searches or by means of accelerators [1].
Direct searches focus on the interaction of a DM candidate $\chi$ with a Standard Model (SM) particle $\Psi$ in the initial state,

$$\chi + \Psi \rightarrow \chi' + \Psi'.$$

Different processes can take place between the DM and SM particles depending on the choice of the detector used to observe the signal. For instance, one could observe a nucleus recoil or an electron recoil (which allows to go lower and lower with DM masses) in the final state.
Indirect searches, instead, start from the interaction of two DM particles and focus on the study of the final SM state:

$$\chi + \chi' \rightarrow \Psi + \Psi'.$$

In particular, when performing these type of searches, one looks for anomalies in photon, neutrino or cosmic ray fluxes due to the annihilation or decay of DM particles. This flux discrepancy can potentially be observed in SM particle fluxes coming from heavy objects, like galaxies, the Sun or the Earth.
Another possible way to discover DM particles is through colliders or fixed target experiments. The idea is to search for new particles that appear after the interaction of two SM particles,

$$\Psi + \Psi' \rightarrow \chi + \chi',$$

by looking for resonances peaked at the mass of the new particle or by calculating the missing energy in the final state. Contrary to direct and indirect searches, one always needs to compare the accelerator results with Astroparticle experiments to be sure that $\chi$ is indeed the desired DM constituent and not another new particle. [2]

In general, DM candidates must be weakly interacting, massive and stable particles to account for the correct DM density in the Universe. In this scenario, SuperWIMPs (Weakly Interacting Massive Particles) could represent the desired keV-scale particle content of DM, arising in well-motivated theoretical frameworks. Using the data collected by the GERDA (GERmanium Detector Array) experiment, one can perform a direct search for SuperWIMPs. Despite the fact that GERDA is dedicated to the search for the neutrinoless double-beta decay expected at $Q_{\beta\beta} \sim 2039$ keV, one can exploit the low energy data to set constraints on the pseudoscalar ($g_{ae}$) and vector ($\alpha/\alpha'$) SuperWIMPs coupling strengths to SM particles. This analysis can be performed thanks to the employment of an array of high-purity Germanium detectors enriched in $^{76}$Ge that operate in an ultra low background environment at the Laboratori Nazionali del Gran Sasso (LNGS) of Istituto Nazionale di Fisica Nucleare (INFN) in Italy. Since SuperWIMPs interact via a sort of photoelectric effect inside the Germanium detectors by releasing an electron in the final state, one can perform a generic peak search all through the energy

spectrum in order to spot a signal excess over the continuum background. If an excess is observed and it is not related to any known background source (e.g. $\beta$ or $\gamma$ decays), one will claim the discovery of new physics. On the other hand, if no excesses are found or there is an excess that can be explained with the presence of a nearby background source, one will set upper limits for the signal counting rate.

In particular, the thesis work consists of performing a Bayesian analysis to search for bosonic SuperWIMPs inside the mass range $[60; 1000]$ keV/c$^2$, as done in Ref. [3]. In the previous work, upper limits for SuperWIMPS coupling strengths to electrons were extracted using GERDA Phase II data (December 2015 - April 2018). Two types of detectors were used, i.e. enriched coaxial and Broad Energy Germanium (BEGe) detectors, considering

- 28.2 kg·yr (coaxial), 30.1 kg·yr (BEGe) of exposure for data in the $[200; 1000]$ keV/c$^2$ mass range;
- 6.9 kg·yr (coaxial), 7.7 kg·yr (BEGe) of exposure for data in the $[60; 200]$ keV/c$^2$ mass range

The current work, instead, focuses on the analysis of a larger dataset that is given by Phase II and Phase II+ (July 2018 - November 2019) data. This larger dataset considers

- 41.8 kg·yr (coaxial), 54.9 kg·yr (BEGe) of exposure for data in the $[195; 1000]$ keV/c$^2$ mass range;
- 20.7 kg·yr (coaxial), 30.5 kg·yr (BEGe) of exposure for data in the $[60; 195]$ keV/c$^2$ mass range

Since five Inverted Coaxial (IC) detectors were installed after Phase II, 8.8 kg·yr of exposure were additionally considered for data in the $[60; 1000]$ keV/c$^2$ mass range.

In the following, a brief description is provided for each chapter.

- **Chapter 1** provides a theoretical overview of the DM problem. Explaining the main differences between cold and hot DM, WIMPs and SuperWIMPs candidates are introduced. In particular, the distinction between pseudoscalar and vector SuperWIMPs and the interaction of these DM particles with SM particles are explained. Finally, the formulas for the interaction rate of SuperWIMPs with Earth-bound detectors are shown, as well as the first search for SuperWIMPs made by GERDA together with other direct and indirect searches performed by other experiments.
- **Chapter 2** introduces the GERDA experiment and its search for the neutrinoless double-beta decay. The different Phases and results collected by the experiment are reported, together with the most crucial technologies and tools employed during the years of operation. A brief description of the whole experiment is provided in Sec. 2.1.1. Germanium detectors and their arrangement are shown in Sec. 2.1.2; in Sec. 2.1.3 and 2.1.4, the liquid Argon (LAr) and muon veto systems are described in detail.
- **Chapter 3** is devoted to the description of the analysis procedure. After having introduced the physics problem, the dataset used for the analysis is shown in detail. In Sec. 3.2.2, the Bayesian analysis is explained, as well as the method used to declare a signal excess that can be later justified with the presence of SuperWIMPs in the energy spectrum. Additional details for the Bayesian analysis can be found in Sec. 3.2.3 and 3.2.4. Sec. 3.3, instead, is dedicated to the calculation of the total detection efficiency of SuperWIMPs inside Germanium detectors.
- **Chapter 4** shows upper limits for the signal counting rate obtained for each type of detector. In Sec. 4.2, part of the results obtained by analyzing the data collected by GERDA are explained through a Monte Carlo study. Sec. 4.3, finally, shows the limits for SuperWIMPs coupling strengths to electrons in Germanium Earth-bound detectors.
- **Appendix A** displays Bayesian fits to real data for energies at which an excess was observed.
- **Appendix B** shows the channel, total and active mass, and exposure level for each type of detector used during GERDA Phase II and Phase II+.

# Chapter 1

# Search for SuperWIMPs

## 1.1 Dark Matter and SuperWIMPs

DM constitutes about 27% of our Universe, together with 68% of dark energy and 5% of ordinary matter. With DM, one usually refers to matter made up of particles that do not interact via electromagnetic interactions. Thus, the spectroscopic observation of this different form of matter is forbidden since DM is not able to scatter photons. [1]
Starting from cosmological nucleosynthesis arguments related to the primordial abundances of light elements, DM was found to be present in two different forms, i.e. in a "baryonic" and "non-baryonic" form. Recently, non-baryonic DM was discovered to be further divisible into a "hot" and a "cold" component. These two types of non-baryonic DM lie at different mass scales equal to $M_{HDM} \approx 10 - 100$ eV and $M_{CDM} \approx 10 - 30$ GeV, respectively. Thus, hot constituents tend to move ultra-relativistically, while cold candidates tend to move slower for equal energy values. This difference is mainly related to a thermal relic phenomenon, for which particles stop to contribute to the interaction processes happening in the Universe, reaching, in the end, a constant abundance. Depending on the time, i.e. the temperature $T_F$, at which these particles froze out, the final density changes.
Being the abundance of a field equal to $\Omega_X = \rho_X/\rho_0$, where $\rho_X$ is the density associated to the field $X$ and $\rho_0 \approx 10^{-29}\, g/cm^3$ (i.e. about 10 protons per cubic meter) is the present energy density of the Universe, then:

- if particles were relativistic when they stopped to annihilate (i.e. $T_F > m$, where $m$ is the particle rest mass), their current number density should be comparable to that of the microwave background photons, which means that the relic density parameter should be equal to $\Omega_{HDM} \approx (m/100\,\text{eV})$;

- instead, if particles were non-relativistic when they froze out (i.e. $T_F < m$), their relic density parameter should decrease with the particle mass due to Boltzmann suppression, $\Omega_{CDM} \sim m^{-1.9}$.

The current SM of Cosmology, i.e. the ΛCDM model, believes that DM is mainly made up of cold DM. In the ΛCHDM model, a hot component is considered as well. [4]
The leading class of candidates for cold DM are WIMPs, i.e. particles that are thought to interact in a weak and renormalizable way with SM particles. WIMPs have no reasons for being fully stable, and they can later decay into SuperWIMPs, which tend to have an interaction rate much weaker than weak interactions. The main difference between these two classes of particles resides in their couplings to ordinary matter (which is higher for WIMPs with respect to SuperWIMPs), while their relic density must be similar since SuperWIMPs are the decay products of WIMPs. [5]
There is also the possibility that cold DM may be somewhat lighter with $M_{CDM} \sim \mathcal{O}(10 - 100)$ eV. Having masses at the keV scale means a weaker coupling to SM particles caused by an earlier thermal decoupling that took place at lower temperatures. Despite this, the correct DM energy density remains ensured. [6]

## 1.2 Axion-Like Particles and Dark Photons

As the nature of DM remains a mystery, DM may be made up of particles that belong to a new hidden, dark sector (DS). Since the DS is assumed to exist as a world parallel to our own, a way for these two sectors to enter into contact is through a *portal*, i.e. a weakly interacting massive particle that acts as the mediator between the two. Portals can take various forms that can be classified by the dimension of their operators or according to the spin of the mediator field. [7]
Concerning SuperWIMPs, three types of candidates have been suggested: scalar, pseudoscalar and vector particles. Only pseudoscalar and vector SuperWIMPs are presented in the following, since the phenomenology of scalar SuperWIMPs tend to be very complex.

Pseudoscalar SuperWIMPs belong to the class of Axion-Like Particles (ALPs). Axions are ultra-light bosons that were hypothetically introduced to explain a possible violation of the parity (P) and charge conjugation-parity (CP) in strong interactions. However, differently from QCD axions, ALPs are not associated with the strong CP problem since they do not interact via the strong force. The Lagrangian term for the interaction of ALPs with SM photons is given by

$$\mathcal{L}_{ALP} = \frac{1}{2}\partial_\mu a\, \partial^\mu a - \frac{1}{2}m_a^2\, a^2 - \frac{1}{4}g_{a\gamma\gamma} a F_{\mu\nu}\widetilde{F}^{\mu\nu} \tag{1.1}$$

where $a$ is the ALP field and $m_a$ the corresponding mass, $F_{\mu\nu}$ is the electromagnetic field-strength tensor ($\widetilde{F}^{\mu\nu} = \varepsilon^{\mu\nu\rho\sigma}F_{\rho\sigma}$), while $g_{a\gamma\gamma}$ is the coupling of ALPs to SM photons. The photon coupling $g_{a\gamma\gamma} = r\alpha/(2\pi f_a)$ is related to the ALP decay constant, $f_a$; $r$ is a model-dependent constant expected to be $\mathcal{O}(1)$ and usually set equal to 1. Hence, the free parameters that enter in the Lagrangian are $m_a$ and $f_a$. [8]

Vector SuperWIMPs, also known as dark photons (DPs), couple to the SM sector through a kinetic mixing term. In particular, this term mixes a dark gauge field with one visible Abelian gauge boson, giving rise to the final four-dimensional operator. One of the most general and popular models for DPs is:

$$\mathcal{L}_{DP} = \mathcal{L}_{SM} + \mathcal{L}_{DS} - \frac{\hat{\epsilon}}{2}V^{\mu\nu}X_{\mu\nu} + \frac{1}{2}m_{A'}^2 A'_\mu A'^\mu \tag{1.2}$$

where the SM and DS Lagrangian terms are given by

$$\mathcal{L}_{SM} = -\frac{1}{4}V_{\mu\nu}^2 + \bar{\psi}\left[\gamma_\mu\left(i\partial_\mu - \tilde{e}\tilde{A}_\mu\right) - m_\psi\right]\psi \tag{1.3a}$$

$$\mathcal{L}_{DS} = -\frac{1}{4}X_{\mu\nu}X^{\mu\nu} + \bar{\chi}\left[\gamma_\mu\left(i\partial_\mu - e' A'_\mu\right) - m_\chi\right]\chi \tag{1.3b}$$

Specifically, $\tilde{A}$ is the visible SM gauge field ($V_{\mu\nu} = \partial_\mu\tilde{A}_\nu - \partial_\nu\tilde{A}_\mu$), $A'_\mu$ is the invisible DP gauge field ($X_{\mu\nu} = \partial_\mu A'_\nu - \partial_\nu A'_\mu$), $e'$ is the dark gauge coupling, $\tilde{e}$ is the SM gauge coupling, $m_{A'}$ is the DP mass, $\chi$ is a DM candidate with mass $m_\chi$, and $\psi$ is a Dirac fermion with mass $m_\psi$.
The kinetic mixing term in Eq. (1.2), i.e. $-\hat{\epsilon}V^{\mu\nu}X_{\mu\nu}/2$, is proportional to the kinetic mixing parameter $\hat{\epsilon}$ which enters the definition of the "millicharge" parameter,

$$\kappa = \epsilon \cdot \frac{e'}{e} = \epsilon \cdot \sqrt{\frac{\alpha'}{\alpha}} \tag{1.4}$$

where $\epsilon = \hat{\epsilon} \cdot cos\,\theta_W$, $\alpha' = {e'}^2/4\pi$ is the hidden sector fine structure constant, and $\alpha$ is the usual electromagnetic fine structure constant. [7, 9]

## 1.3 SuperWIMP Signature

Pseudoscalar and vector SuperWIMPs couple to SM particles through decay (e.g. in two and three photons respectively), emission or absorption processes. Annihilation events are usually studied in

the so-called indirect searches, whereas the so-called direct searches are based on the scattering of SuperWIMPs in an Earth-bound detector. The corresponding signal can be spotted by measuring the energy deposition in a calorimeter after the SuperWIMP scatters on a nucleus which later recoils, or it can be spotted by looking at the scintillation light or to ionization events. [6]

At GERDA, the leading way in which a SuperWIMP can be detected is through an absorption process. Indeed, SuperWIMPs ($\phi$) can be absorbed by an electron of an outer shell of an atom of the traversed material:

$$\phi + e^- + Z \rightarrow e^- + Z \tag{1.5}$$

The electron in the final state can later deposit its energy in the traversed medium. This phenomenon, also known as the "axio-electric effect" for ALPs, is similar to the usual photoelectric effect produced by a SM photon, generating a full absorption peak in the energy spectrum. Since SuperWIMPs tend to have low kinetic energies, the signature peaks lie at energies equal to the mass of the absorbed particle corrected by the binding energy of the emitted electron.
The Lagrangian for the interaction of a pseudoscalar SuperWIMP with an electron is

$$\mathcal{L}_{ALP,\,e} = g_{ae} a \bar{\psi} i \gamma_5 \psi \tag{1.6}$$

with $g_{ae} = 2m_e/f_a$. This Lagrangian gives the absorption cross section for ALPs, which can be expressed in terms of the usual photoelectric effect cross section $\sigma_{pe}$ evaluated at a photon energy equal to the ALP mass:

$$\frac{\sigma_{ALP,\,abs}}{\sigma_{pe}(\omega = m_a)} \approx g_{ae}^2 \frac{3m_a^2}{16\pi\alpha m_e^2} \cdot \frac{c}{v} \tag{1.7}$$

where $v$ is the SuperWIMP incoming velocity and $c$ is the speed of light.
The Lagrangian for the interaction of a vector SuperWIMP with an electron, instead, is

$$\mathcal{L}_{DP,\,e} = e\kappa A'_\mu \bar{\psi} \gamma^\mu \psi \tag{1.8}$$

The corresponding absorption cross section for DPs is:

$$\frac{\sigma_{DP,\,abs}}{\sigma_{pe}(\omega = m_{A'})} \approx \frac{\alpha'}{\alpha} \cdot \frac{c}{v} \tag{1.9}$$

To calculate the interaction rate of SuperWIMPs within a detector, one must evaluate the count rates obtained in a generic signal peak. The expected interaction rates for pseudoscalar and vector SuperWIMPs in a given detector are obtained by combining the expected flux of those particles with the absorption cross section $\sigma_{abs}$. Considering that the SuperWIMPs local DM density is $\rho_{DM} = 0.3\,\mathrm{GeV}/cm^3$, the interaction rate in a direct detection experiment for a Earth-bound detector is

$$R_{ALP} \approx \frac{1.29 \cdot 10^{19}}{A} g_{ae}^2 \left(\frac{m_a}{[\mathrm{keV/c^2}]}\right) \left(\frac{\sigma_{pe}}{[b]}\right) [kg^{-1}d^{-1}] \tag{1.10}$$

for pseudoscalar SuperWIMPs, and

$$R_{DP} \approx \frac{4 \cdot 10^{23}}{A} \frac{\alpha'}{\alpha} \left(\frac{[\mathrm{keV/c^2}]}{m_{\gamma'}}\right) \left(\frac{\sigma_{pe}}{[b]}\right) [kg^{-1}d^{-1}] \tag{1.11}$$

for vector SuperWIMPs, being $A$ the detector's atomic number. In particular, due to the dependence on the photoelectric cross section, the energy-dependent number of events exhibits the characteristic sawtooth edges in correspondence of the L or K electron shells energies. [6]

Experiments set constraints on the dimensionless coupling strengths of pseudoscalar and vector SuperWIMPs starting from the measurement of their interaction rates within a given material. In Fig. 1.1, measurements performed at different mass values are shown for several experiments. The peculiarity of the GERDA experiment lies in its enhanced sensitivity in setting the coupling strengths limits, which

is due both to the large exposure and the low background rate over all of the search region and to the employment of Germanium detectors, which are characterized by a better energy resolution with respect to other detectors employed by other experiments.

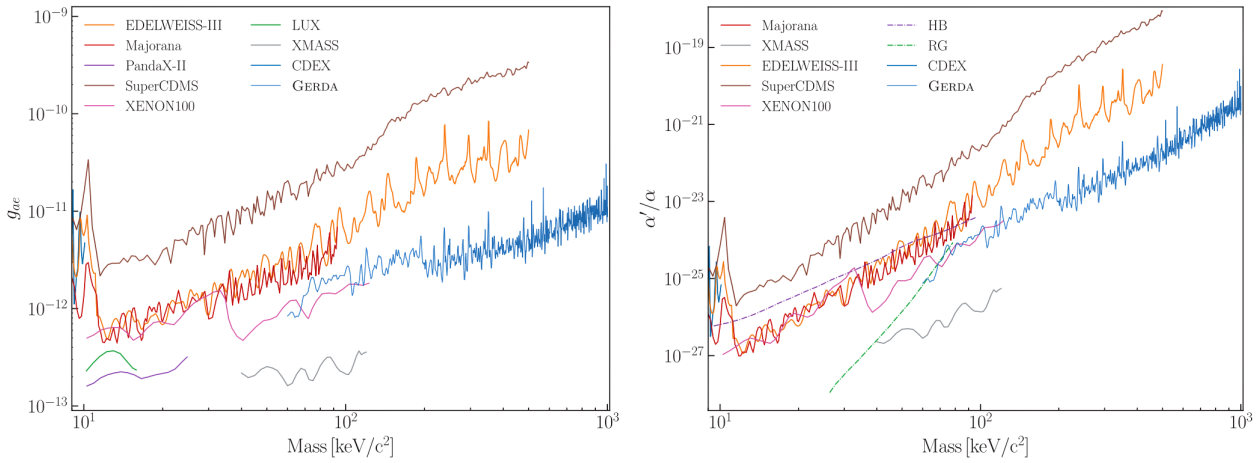


Figure 1.1: detection limits on pseudoscalar ($g_{ae}$, left plot) and vector ($\alpha'/\alpha$, right plot). Results are shown for direct detection studies coming from CDEX, EDELWEISS-III, LUX, the Majorana Demonstrator, PandaX-II, SuperCDMS, XENON100, XMASS and GERDA, and for indirect detection studies coming from horizontal branch (HB) and red giant (RG) stars. [3]

In Tab. 1.1, the detectors used by each direct experiment listed in Fig. 1.1 is provided together with the collected exposure and the analyzed mass range for SuperWIMPs.

| **Experiment** | **Detector** | **Exposure** | **Mass range [keV/c$^2$]** |
|---|---|---|---|
| GERDA [3] | Ge crystals | 14.6 kg · yr | 60 – 200 |
| | | 58.9 kg · yr | 200 – 1000 |
| EDELWEISS-III [10] | Ge crystals | 1149 kg · d | 0.8 – 500 |
| Majorana Demonstrator [11] | Ge crystals | 478 kg · d | 1 – 100 |
| SuperCDMS [12] | Ge crystals | 327.8 kg · d | 0.40 – 500 |
| CDEX [13] | Ge crystals | 335.6 kg · d | 0.475 – 10 |
| PandaX-II [14] | Liquid Xe | $2.7 \cdot 10^4$ kg · d | 1 – 25 |
| XENON100 [15] | Liquid Xe | 224.6 live-days × 34 kg | 8 – 125 |
| LUX [16] | Liquid Xe | 95 live-days × 118 kg | 1 – 16 |
| XMASS [17] | Liquid Xe | 800 live-days × 327 kg | 40 – 120 |

Table 1.1: summary of experiments and their detectors, collected exposure and analyzed mass ranges.

# Chapter 2

# The GERDA Experiment

## 2.1 Design of the GERDA experiment

The GERDA (GERmanium Detector Array) experiment, placed a the LNGS in Italy, was built to unravel the Majorana nature of neutrinos through the observation of the neutrinoless double-beta decay ($0\nu2\beta$). The process violates the total lepton number since two neutrons decay into two protons, releasing only two electrons and no electric neutrinos:

$$(A,\, Z) \rightarrow (A,\, Z+2) \,+\, e^- \,+\, e^- \tag{2.1}$$

In Fig. 2.1, the Feynman diagram of $0\nu2\beta$ decay is shown. The process accounts for the exchange of a light Majorana neutrino interacting via standard, left-handed, V-A weak currents.

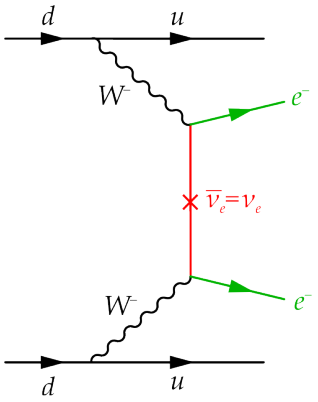


Figure 2.1: Feynman diagram for the neutrinoless double-beta decay.

At GERDA, one investigates the following neutrinoless double-beta decay

$$^{76}_{32}\mathrm{Ge} \rightarrow {}^{76}_{34}\mathrm{Se} + e^- + e^- \tag{2.2}$$

using an array of Germanium detectors placed in a cryostat filled with LAr, which simultaneously shields external radiations and cools the detectors. GERDA data can be separated into two phases:

- Phase I of the experiment lasted from November 2011 to September 2013;
- Phase II, instead, ran from December 2015 to April 2018, when five additional IC detectors were installed for collecting data during Phase II+, which lasted from July 2018 to November 2019.

Results of Phase I were derived for an exposure of 23.5 kg·yr. No signal was found for $0\nu2\beta$ decay, setting thus a lower limit (at 90% C.L.) equal to $T^{0\nu}_{1/2} > 2.1 \times 10^{25}$ yr for the half-life of the $^{76}$Ge decay; the median sensitivity, assuming no signal, was equal to $2.4 \times 10^{25}$ yr. The final results of GERDA on

the search for $0\nu2\beta$ decay were obtained by combining the result of Phase I with Phase (II, II+) data, for a total exposure of 127.2 kg·yr. Assuming no signal, the sensitivity on the half-life limit increased by about one order of magnitude, reaching, in the end, a lower limit of $T^{0\nu}_{1/2} > 1.8 \times 10^{26}$ yr, which coincides with its sensitivity. [18]
To reach this ultimate goal, one must enter the "background-free" regime in the region of interest (ROI) around $Q_{\beta\beta} \sim 2039$ keV, i.e. the background contribution must be less than 1 event in $Q_{\beta\beta} \pm 0.5$ FWHM for the entire period of data-taking. In this case, as shown in Fig. 2.2, the sensitivity grows linearly with exposure $\xi = M \cdot t$, where $M$ is the detector mass and $t$ is the measurement time. In particular, the full behaviour of the half-life sensitivity is

$$T^{0\nu}_{1/2} \propto \begin{cases} \epsilon \cdot f \cdot \sqrt{\frac{\xi}{(\mathrm{BI} \cdot \Delta E)}} & \text{with background} \\ \epsilon \cdot f \cdot \xi & \text{without background} \end{cases} \tag{2.3}$$

where $\epsilon$ is the overall detection efficiency, $f$ is the abundance of $^{76}$Ge, BI is the background index and $\Delta E$ is the energy resolution at $Q_{\beta\beta}$. Eq. (2.3) shows how the half-life sensitivity is strongly modified by the background contribution. The goal for Phase II was to reduce the BI below $10^{-3}$ cts/(keV · kg · yr) to reach the desired sensitivity beyond $10^{26}$ yr at an exposure of 100 kg·yr. Actually, GERDA reached a lower background value of BI $= 5.2^{+1.6}_{-1.3} \times 10^{-4}$ cts/(keV · kg · yr).

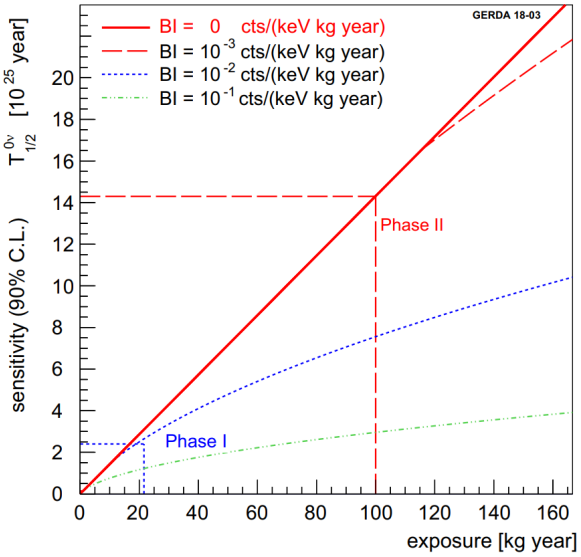


Figure 2.2: GERDA sensitivity for $T^{0\nu}_{1/2}$ as a function of the exposure for different BI values. [19]

To reach the background-free regime, the main changes exploited for Phase II regarded:

- the instrumentation of the LAr with Photomultiplier Tubes (PMTs) and scintillating fibers read-out by Silicon Photo-Multipliers (SiPMs) to detect scintillation light in proximity of the Germanium array;
- the deployment of 20 kg of enriched BEGe detectors.

Indeed, the analysis of Phase I data showed that most of the background events were due to radioactive isotopes inside materials close to the detectors. Thus, these materials were reduced in quantity and/or replaced by other materials having higher radiopurity.
The highest BI reduction, however, is performed through an event selection based on the coincidences of scintillation light in the LAr, on the coincidences within the detector array and/or on the analysis of the signal pulse shape. Indeed, background events tend to deposit energy at several locations (e.g. at the detector surface or in the LAr around the detector) and to scatter, while $0\nu2\beta$ events usually deposit energy within small volumes of about few mm$^3$. [19]

### 2.1.1 General Layout

The GERDA experiment is placed 1400 metres below the surface (i.e. at a depth of 3500 metres water equivalent), both to passively remove the hadronic component of cosmic ray showers and to reduce the muon flux to $\sim 1.25/(\mathrm{m}^2 \cdot \mathrm{h})$. The core of the experiment is an array of Germanium detectors which is lowered inside a stainless steel cryostat (internally covered with Copper). The cryostat is filled with 64 $\mathrm{m}^3$ of liquid Argon and placed inside a water tank containing 590 $\mathrm{m}^3$ of ultra-pure water, where the latter acts as an additional passive shield. Indeed, together with 66 PMTs, water helps to detect those muons that are sufficiently energetic to penetrate inside the experimental setup.
On top of the cryostat and water tank, there is the clean room that protects the detectors against dirt containing natural radioactivity that can be introduced during the installation phase. The clean room also houses a glove box and the lock for assembly and deployment of the Germanium detectors and calibration sources.
The whole experiment is designed in such a way to reduce as much as possible the background contributions, which can be made of cosmic rays, neutrons, gamma rays emitted from the surrounding rocks, support materials, radioactive elements inside LAr (e.g. $^{39,42}$Ar). In addition to these, one has also to take into account the internal background of Germanium diodes. The main internal background component is the double-beta decay ($2\nu2\beta$) of $^{76}$Ge. Another internal background source is related to cosmogenically produced long-lived isotopes such as $^{68}$Ge and $^{60}$Co having half-lives of 270.93 (13) d and 5.2711 (8) yr respectively. Their contribution, also known as "cosmogenic background", is quite negligible. Indeed, by simulating the expected detector bulk impurities around $Q_{\beta\beta}$, their contribution was found to be less than $10^{-4}$ cts/(keV $\cdot$ kg $\cdot$ yr). This result was obtained minimizing the exposure to the cosmic rays firstly of the enriched germanium material then the detectors themselves. A schematic view of the GERDA setup during Phase II can be seen in Fig. 2.3. [19, 20]

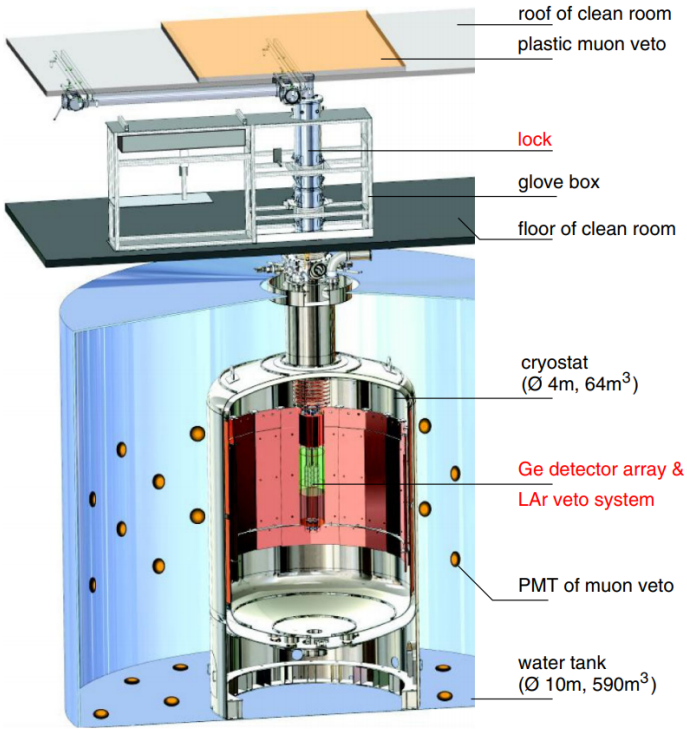


Figure 2.3: experimental setup for GERDA Phase II (December 2015 - April 2018). New components with respect to Phase I (November 2011 - September 2013) are labelled in red. [19]

### 2.1.2 Germanium Detectors

In Fig. 2.4, the Phase II detector arrangement is displayed. Here, 30 enriched BEGe detectors were employed, 21 with a cylindrical shape and 9 with a conical shape; in general, their performances were found to be independent of their shape. One BEGe detector (GD02D), however, is more a pn junction

rather than a p-type detector. Thus, since it does not exhibit full charge collection, it is used only in anti-coincidence (AC) mode. In addition to BEGe detectors, 7 enriched coaxial detectors and 3 coaxial detectors having a natural isotopic abundance of $^{76}$Ge ($f_{76} = 7.8\%$) were also employed. The total mass for enriched detectors is 35.6 kg, while for naturally enriched detectors is 7.6 kg.
In particular, blue-coloured detectors in Fig. 2.4 carry the manufacturer's passivation on the insulating groove between the p+ and n+ contact; the yellow-coloured ones, instead, have this layer removed. The figure also shows where the Silicon plates (horizontal grey lines) are placed. These plates hold the vertical Copper bars that carry the Ge detectors, but they also provide the substrate onto which signal readout and high voltage cables are attached.
After the upgrade, 5 new IC detectors (IC48B, IC50B, IC48A, IC50A, IC74A) were introduced for a total mass of 9.6 kg. Instead, all naturally enriched coaxial detectors and one enriched coaxial detector (ANG1) were removed. The new IC detectors are preferable since they combine the large mass of the traditional coaxial detectors (having an average mass equal to about 2 kg) with the superior energy resolution and Pulse Shape Discrimination (PSD) properties of BEGe detectors. However, IC48B could not be fully depleted due to the high leakage current shown over the entire data taking. It was used only in AC mode.

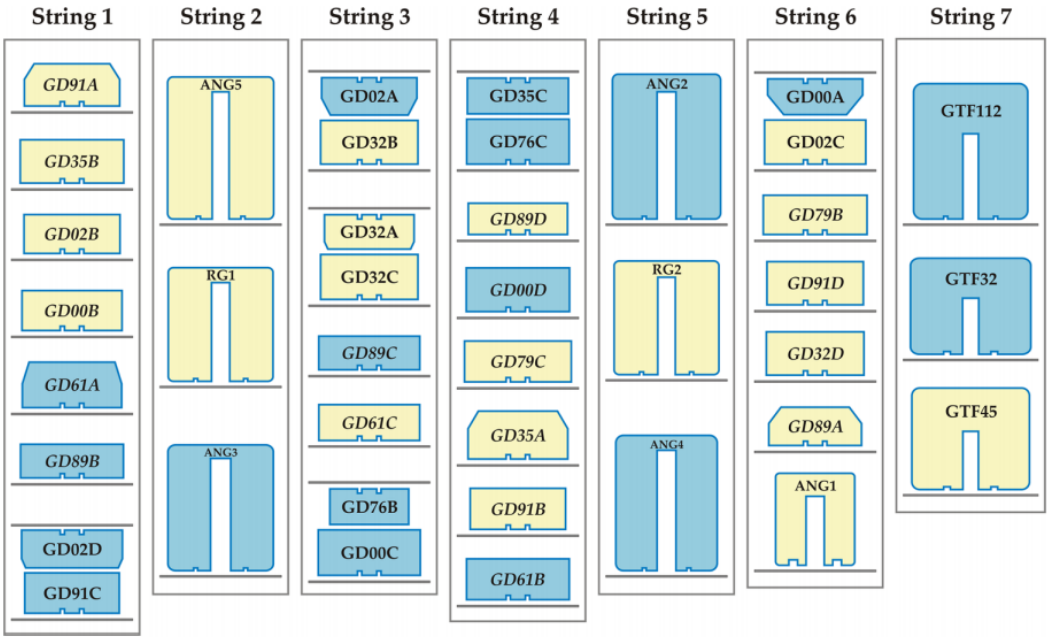


Figure 2.4: distribution of enriched BEGe (GDxxx), enriched coaxial (RGx and ANGx) and natural coaxial (GTFxx or GTFxxx) detectors arranged in seven strings for GERDA Phase II.
Detectors are numbered from 0 (GD91A) to 39 (GTF45) starting from top to bottom, string by string. [19]

Fig. 2.7.b shows the Ge detector array together with the electronic front end boards on top at about 30 cm distance. The height of the array is 40 cm, while its diameter is about 30 cm. Each string of detectors is enclosed by a transparent "mini-shroud" (MS), i.e. a 125 $\mu$m thick cylinder made of nylon introduced to stop the drift of $^{42}$K ions towards the detectors. Since nylon is almost opaque for the UV radiation which is generated inside the LAr, the nylon is covered on both surfaces with a wavelength shifter, which shifts wavelengths from 128 nm to 450 nm. The shifting allows first of all the transport of the scintillation light through the MS, and then its detection by the SiPMs of the LAr veto.
The main properties of the HPGe detectors for Phase II and its upgrade are summarized in Tab. 2.1. The efficiencies of muon veto and quality cuts, which are not shown, are above 99.9%.

To preserve the excellent energy resolution of the HPGe detectors when combining data over a long period of time, a calibration procedure is performed weekly using $^{228}$Th as a radioactive $\gamma$ source. To lower the sources inside the cryostat, three individual units are mounted on the top flange of the lock. They are arranged in such a way to place the sources into the space between the cylinder of the LAr veto system and two neighboring outer string of the detector array. Indeed, the three units

are arranged on a mounting circle of 380 mm diameter at an angular distance of 120° (see Fig. 2.5). During a calibration procedure, a test pulse is injected every 2 s into the amplifier electronics of all HPGe detectors to monitor their gain stability; during the regular operation, instead, test pulses are injected every 20 s. Data with short-term instabilities are discarded from further analysis.

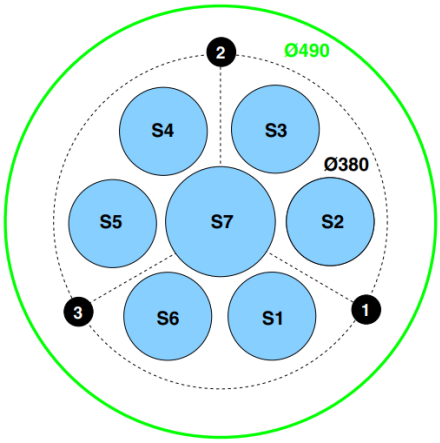


Figure 2.5: schematic view of the top of the Germanium array. Light blue circles represent strings, while black circles (1, 2, 3) represent the positions of the calibration sources. The LAr veto system boundary is shown in green (⌀490 mm). [19]

| | December 2015 - May 2018 | | July 2018 - November 2019 | | |
|---|---|---|---|---|---|
| | Coaxial | BEGe | Coaxial | BEGe | IC |
| Number of detectors | 7 | 30 | 6 | 30 | 5 |
| Total mass | 15.6 kg | 20 kg | 14.6 kg | 20 kg | 9.6 kg |
| Exposure $\xi$ | 28.6 kg · yr | 31.5 kg · yr | 13.2 kg · yr | 21.9 kg · yr | 8.5 kg · yr |
| Energy resolution at $Q_{\beta\beta}$(FWHM) | $(3.6 \pm 0.2)$ keV | $(2.9 \pm 0.3)$ keV | $(4.9 \pm 1.4)$ keV | $(2.6 \pm 0.2)$ keV | $(2.9 \pm 0.1)$ keV |
| $0\nu2\beta$ decay detection efficiency $\epsilon$ : | $(46.2 \pm 5.2)\%$ | $(60.5 \pm 3.3)\%$ | $(47.2 \pm 5.1)\%$ | $(61.1 \pm 3.9)\%$ | $(66.0 \pm 1.8)\%$ |
| Electron containment | $(91.4 \pm 1.9)\%$ | $(89.7 \pm 0.5)\%$ | $(92.0 \pm 0.3)\%$ | $(89.3 \pm 0.6)\%$ | $(91.8 \pm 0.5)\%$ |
| $^{76}$Ge enrichment | $(86.6 \pm 2.1)\%$ | $(88.0 \pm 1.3)\%$ | $(86.8 \pm 2.1)\%$ | $(88.0 \pm 1.3)\%$ | $(87.8 \pm 0.4)\%$ |
| Active volume | $(86.1 \pm 5.8)\%$ | $(88.7 \pm 2.2)\%$ | $(87.1 \pm 5.8)\%$ | $(88.7 \pm 2.1)\%$ | $(92.7 \pm 1.2)\%$ |
| LAr veto | $(97.7 \pm 0.1)\%$ | | | $(98.2 \pm 0.1)\%$ | |
| PSD | $(69.1 \pm 5.6)\%$ | $(88.2 \pm 3.4)\%$ | $(68.8 \pm 4.1)\%$ | $(89.0 \pm 4.1)\%$ | $(90.0 \pm 1.8)\%$ |

Table 2.1: GERDA parameters for different detectors before and after the Phase II upgrade (April 2018). [18]

In Fig. 2.6, the energy distribution between 1 MeV and 5.2 MeV is shown for a total acquisition of 103.7 kg·yr corresponding to data acquired in Phase II and II+, i.e. between December 2015 and November 2019. Data are shown both before the analysis cuts and after them.

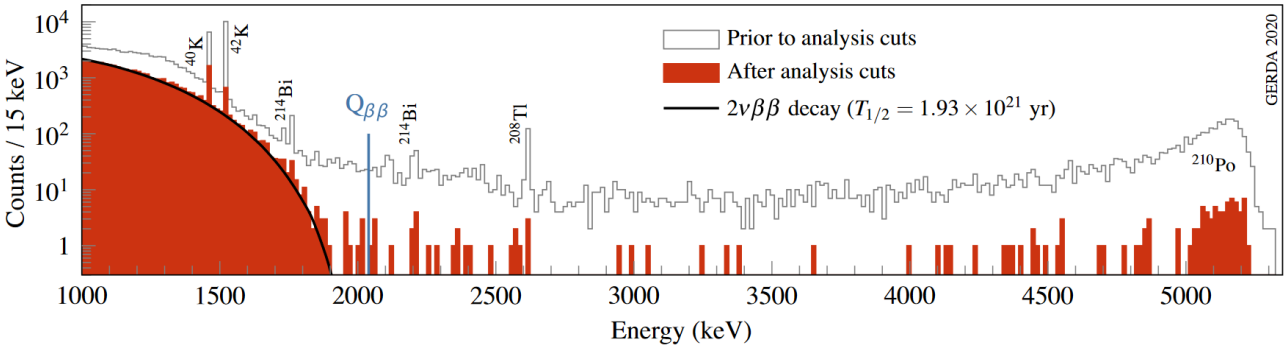


Figure 2.6: energy distribution of Phase II events (103.7 kg·yr) before and after analysis cuts. The expected distribution of $2\nu2\beta$ decay events is shown assuming the half-life measured by GERDA. [18]

### 2.1.3 LAr Veto System

The LAr veto system was designed to detect background events produced in proximity of the HPGe detectors. The Argon scintillation light events are usually multi-site events generated by $\gamma$ rays coming from Ra and Th decays in solid materials inside and around the detectors, by muons or by decays from $^{42}$Ar and $^{42}$K.
The LAr veto system has a cylindrical shape with a diameter of $\sim 0.5$ m and a total length of $\sim 2.6$ m. It consists of a curtain of wavelength-shifting fibers connected to $3 \times 3$ mm$^2$ SiPMs and 16 cryogenic PMTs (9 on the top, 7 on the bottom) as shown in Fig. 2.7.a. The geometric coverage of the fibers was improved during the upgrade in order to achieve the largest possible coverage and, at the same time, to use the minimum amount of material to minimize the radioactivity around the HPGe detectors. The fibers are held in place by Copper holders and supported by a Copper frame that carries also the weight of the bottom PMTs. [18, 19]

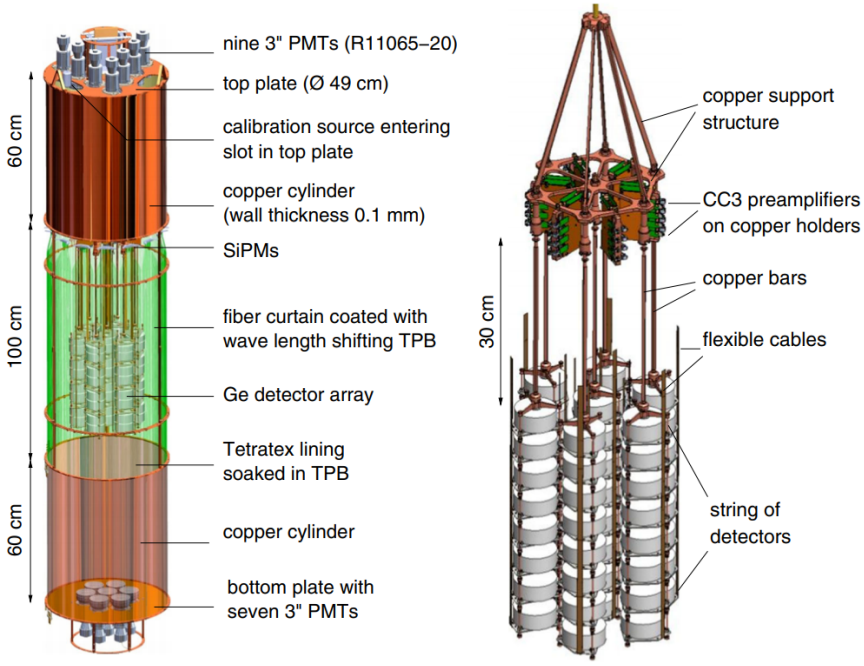


(a) LAr veto system (b) Detector array

Figure 2.7: GERDA Phase II schematic view for LAr veto system (a) and arrangement of Germanium strings and preamplifiers (b). [19]

### 2.1.4 Muon Veto System

A muon veto system was built to exclude energetic muons that enter inside the GERDA experiment without being previously stopped in the surrounding rocks. Muons, indeed, can lose energy both by electromagnetic interactions and by inelastic reactions with nuclei, hence producing high energy neutrons. In order to spot muons, the water tank together with the PMTs are used; in particular, one looks for the Cherenkov light emitted by these particles inside the water tank. To increase the light collection efficiency and to shift UV light into visible light, a reflective 206 $\mu$m thick foil was glued on the inner walls of the water tank, its floor and the outer surfaces of the cryostat. Since muons can also pass through the neck of the cryostat, an array of plastic scintillators, which are placed on the roof of the clean room, was adopted. [21]

# Chapter 3

# Analysis of Data Collected by GERDA

## 3.1 Search for SuperWIMPs at GERDA

Events collected by GERDA in Phase II and Phase II+ are used to perform a generic peak search analysis by looking for monoenergetic signals with a sharp peak signature. With such a study, one aims to detect or set an exclusion limit on the type of interactions that can give rise to a Gaussian peak in the GERDA energy spectrum. The Bayesian analysis applied in this study enables the search for rare events, such as the interactions of SuperWIMPs with HPGe detectors. Indeed, the union between a high energy resolution and a high background reduction (also achievable thanks to the use of active techniques in data selection) helps GERDA to investigate other rare phenomena characterized by energies ranging from few keV up to 5000 keV and over. In particular, the SuperWIMP analysis is limited to the range $[60; 1000]$ keV. The lower and upper limits of this range are justified by the following arguments:

- the lower limit is set at 60 keV because of the trigger threshold (see Sec. 3.2.1) and of the width chosen for the fit window (see Section 3.2.3).
- the upper limit is set at 1000 keV since at masses larger than twice the electron mass, vector SuperWIMPs are expected to annihilate into $e^+e^-$ pairs with lifetimes which are too short to account for the DM.

The novelty of GERDA consists in exploring mass values up to 1 MeV, overcoming the limit at about 500 keV of other direct and indirect searches like Majorana, XENON100, SuperCDMS and many others (see Fig. 1.1). To search for SuperWIMPs, one has to look for Gaussian peaks characterized by a width equal to the energetic resolution of the HPGe detectors. The main advantages of GERDA are the ultra-low background in most of the energy coverage and the excellent energy resolution provided by the enriched Germanium detectors.

## 3.2 Analysis Procedure

### 3.2.1 Physics Dataset

The search for SuperWIMP signals is done on data collected between December 2015 and April 2018 (Phase II, run $53 - 93$), plus data collected between July 2018 and November 2019 (Phase II+, run $95 - 114$). However, some runs were neglected in the final dataset: indeed, in run 66 and 68, the muon veto and the test pulses were not active, respectively; run 80 was acquired after a water tank drainage; run 81 and 82 had an increased rate of accepted events; run 102 is a calibration run.
Before performing the analysis, the dataset was cleaned by applying several cuts to discard non-physical events and consider only monoenergetic signals in the energy spectra. In particular, some quality cuts were applied to remove test pulse, baseline, pile-up's events. Then, events having a multiplicity higher than one, i.e. events where more than one detector is fired, were discarded. Finally, muon-induced

events (which are revealed through the muon veto) or LAr scintillation events (which are detected through the LAr veto) were also rejected.
Actually, one could create the energy spectra in a manner that PSD cuts can be applied too. However, PSD cuts are crucial for the neutrinoless double-beta decay analysis, while, for energies below 1 MeV, they are a subject of study. For this reason, PSD cuts were neglected in the current analysis.

In Fig. 3.1, the energy spectrum for each type of detector is shown together with the position of the $Q_{\beta\beta}$ value at 2039 keV, the $^{76}$Ge double-beta decay ($2\nu2\beta$) and some background lines. Notice that the amount of $^{39}$Ar $\beta^-$ decay inside the energy spectrum is higher for enriched coaxial detectors than for BEGe and IC ones because of the larger surface area of the signal read-out electrodes of the former (see also Fig. 3.2). At higher energies, i.e. at around 5.3 MeV, there is also a peak-like signature with a low energy tail. This structure is attributable to $\alpha$ particles coming from the $^{210}$Po decay on the thin detector $p^+$ surfaces. [20]

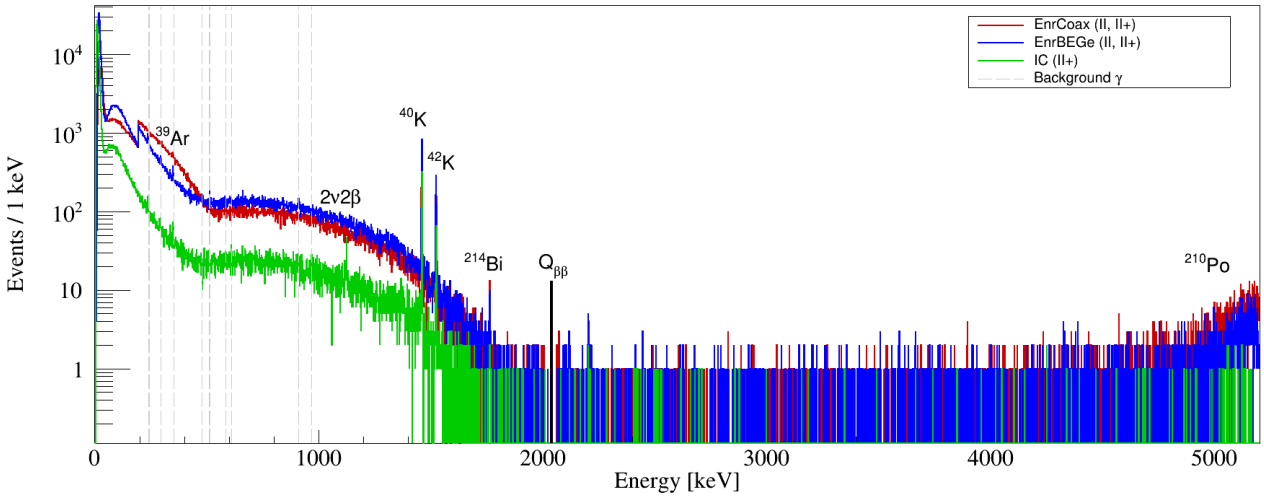


Figure 3.1: energy spectrum for enriched coaxial detectors (red), BEGe detectors (blue) and IC detectors (green). Grey-dashed lines represent $\gamma$ lines for energies below 1000 keV (see Tab. 3.3).

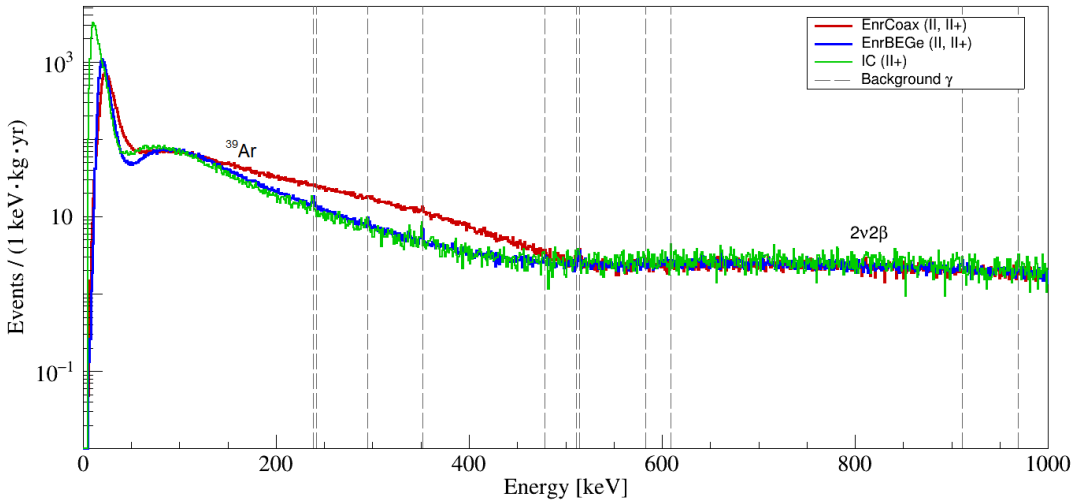


Figure 3.2: energy spectrum normalized by exposure (see Tab. 3.1) for energies up to 1 MeV.

At 195 keV, a clearly visible jump is present in BEGe and coaxial detectors spectra. Indeed, before October 2017 (run 53-86), these detectors had high energy thresholds, because of which one must accept events having sufficiently high energies (i.e. higher than 195 keV). Then, their energy threshold was lowered from about 140 keV to 40 keV, allowing to accept data that have also been collected below

195 keV. Thus, depending on the energy, different levels of exposure were collected. In Tab. 3.1, the summary of the analyzed datasets, the energy ranges and the exposures are shown.

| **Dataset** | **Range [keV]** | **Exposure [kg · yr]** | | |
|---|---|---|---|---|
| | | **Coax** | **BEGe** | **IC** |
| Mini-set | 60 − 195 | 20.7 | 30.5 | |
| Phase (II, II+) | 195 − 5200 | 41.8 | 54.9 | |
| Phase (II+) | 60 − 5200 | | | 8.8 |

Table 3.1: exposure of the analyzed datasets.

### 3.2.2 Bayesian Analysis

The analysis of this work was performed thanks to the BAT (Bayesian Analysis Toolkit [22]) software package, which helps to solve statistical problems in Bayesian inference by using a Markov Chain Monte Carlo (MCMC) based on the Metropolis algorithm. In general, starting from Bayes' theorem with given data $E$ and a model $M$, the probability for the signal counting rate $R$ is given by:

$$P(R,\theta|E,M) = \frac{P(E|R,\theta,M)\,\pi(R)\,\pi(\theta)}{\int\int P(E|R,\theta,M)\,\pi(R)\,\pi(\theta)\,dR\,d\theta} \tag{3.1}$$

where $P(E|R,\theta,M)$ is the conditional probability (or likelihood), whereas $\pi(R)$ and $\pi(\theta)$ are respectively the prior probabilities for the signal count rate and nuisance parameters, both estimated before the fit. In other words, the knowledge about the model before the experiment ($\pi(R)\,\pi(\theta)$) is updated using the probability of new data for different values of the parameters ($P(E|R,\theta,M)$), resulting in posterior knowledge ($P(R,\theta|E,M)$).
The key points for the Bayesian analysis performed through the BAT software are the following ones:

1. primary parameters of interest are added to a model;
2. uniform priors are adopted for each parameter of interest by defining them inside an accurately chosen range;
3. a likelihood function is defined according to Eq. (3.5) or (3.9).

In particular, the mathematical form of prior distributions was chosen to be constant over a given range to add no information to the Bayesian inference. In this way, a parameter of interest can assume each possible value of the specified range with equal probability.
After each Bayesian fit, the final value for a parameter of interest is given as the global mode of the corresponding marginal distribution. For instance, the posterior marginalized distribution for the signal counting rate is given by

$$P(R|E,M) = \int P(R,\theta|E,M)\,d\theta \tag{3.2}$$

To get sufficiently smooth marginal distributions by simultaneously keeping as low as possible the running time, the precision of the generated Markov chains was set to `kHigh`. In this case, eight Markov chains (each having $10^6$ iterations) were generated since, for non-infinite long chains, the final output depends on the initial point.

For SuperWIMPs, once the global mode is extracted for the signal counting rate, one can draw conclusions by comparing this value to the standard deviation of the respective posterior marginalized distribution. The standard deviation is firstly defined as

$$\sigma = U_{34.15} \tag{3.3}$$

where $U_{34.15}$ is the quantile value such that the area subtended between the mode and this value represents 34.15% of the total area of the posterior distribution. If the global mode is not compatible with zero counts within one standard deviation, the latter is defined in a different way, i.e. as

$$\bar{\sigma} = \frac{U_{68} - L_{68}}{2} \tag{3.4}$$

where $U_{68}$ and $L_{68}$ are the upper and lower 68% quantile values extracted from the signal counting rate posterior marginalized distribution. If the mode is higher than $5\bar{\sigma}$, i.e. above zero counts, and there are no background $\gamma$ lines nearby the fit window, signal detection is claimed and the mode with the error estimated with the 68% quantile is quoted. Otherwise, if no excesses are found, a 90% credible interval (C.I.) upper limit on the signal strength must be set. In general, an upper limit is set irrespective of the global mode of the signal counting rate if the Bayesian fit is performed for energy that lies within five times the energy resolution from a known $\gamma$ line.

### 3.2.3 Fit Model

The fit procedure consists in creating an energy window of 24 keV in width inside which a fit is performed, considering a bin width for the energy spectrum equal to 1 keV (i.e. $1\sigma$ energy resolution). This window will be shifted to higher energies from 60 keV up to 1000 keV by steps of 1 keV to search for possible Gaussian signal peaks and to examine each possible mass value. These unexpected signals can be associated to the presence of a SuperWIMP having a mass exactly equal to the centroid of the signal.
Supposing that the fit window is centered at an energy equal to $E_0$, the total fit model must include a term which refers to the Gaussian SuperWIMP signal (modulated by the energetic resolution of the Germanium detectors) and a term which refers to the underlying background. The latter, in particular, is chosen differently depending on the energy range in which the fit is performed: for low energies, i.e. below 195 keV, the background is chosen as a second-order polynomial; otherwise, the background is chosen as a first order polynomial. Thus, the total energy-dependent fit function is:

$$M_0(E) = B(E) + \mathcal{G}\left(\mathcal{N},\, E_0,\, \sigma\right) \tag{3.5}$$

where $B(E)$ is the background polynomial, $\mathcal{N}$ is the number of counts under the signal peak, $E_0$ is the mass of SuperWIMPs and $\sigma$ is the effective resolution of detectors. The latter is known from the calibration data and is equal to:

$$\sigma(E) = \sqrt{a + b \cdot E} \tag{3.6}$$

It is an energy dependent function where $a$ and $b$ are fit parameters: $a$ takes into account contributions coming from electronic noise, whereas $b$ takes into account contributions coming from statistical fluctuations in the number of charge carriers. The fit parameters are shown in Table 3.2 for each detector type. In Fig. 3.3, the behaviour of the FWHM values - obtained starting from Eq. (3.6) - is displayed for energies between 60 and 1000 keV.

| **Detector** | **a [keV$^2$]** | **b [$10^{-4}$ keV]** |
|---|---|---|
| Coaxial | 0.985 (2) | 10.73 (2) |
| BEGe | 0.551 (1) | 4.294 (9) |
| IC | 0.280 (2) | 5.83 (2) |

Table 3.2: resolution curves parameters obtained for each type of detectors. [23]

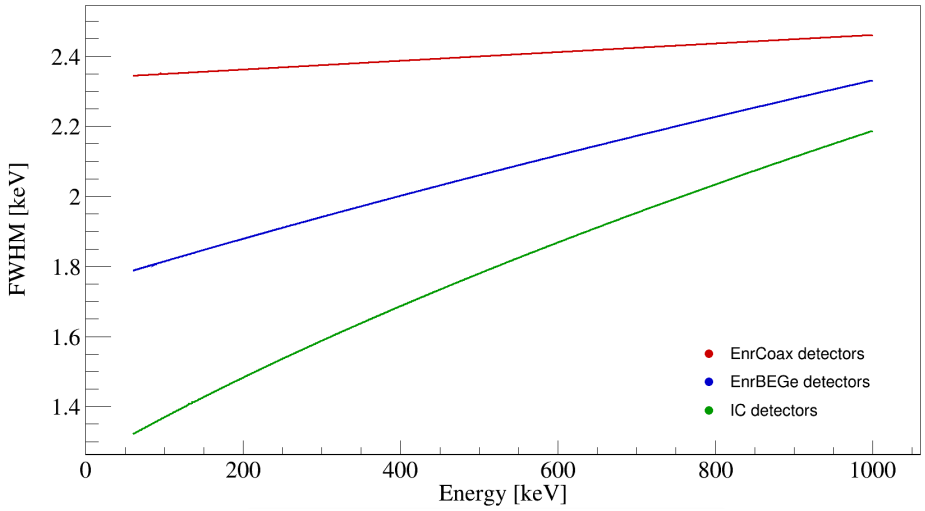


Figure 3.3: FWHM as a function of the energy for each type of detectors.

As regards the background term, the parametrization of the linear function

$$B(E) = m \cdot (E - E_0) + q \tag{3.7}$$

was chosen in a way that reduces the correlation between the slope and offset values to enhance the Bayesian fit stability. The parametrization of the quadratic function

$$B(E) = r \cdot (E - E_0)^2 + s \cdot (E - E_0) + t \tag{3.8}$$

was derived accordingly. The background, however, can also include $\gamma$ lines. In the energy range of interest, electromagnetic transitions having branching ratios higher than 0.1% are taken into account (see Tab. 3.3) since they can occasionally enter into play in the fit window. Thus, the most general form for the fit function is:

$$M_1(E) = M_0(E) + \mathcal{G}(\mathcal{N}_1, E_1, \sigma_1) + \mathcal{G}(\mathcal{N}_2, E_2, \sigma_2) \tag{3.9}$$

where $\mathcal{G}(\mathcal{N}_1, E_1, \sigma_1)$ and $\mathcal{G}(\mathcal{N}_2, E_2, \sigma_2)$ models two possible $\gamma$ lines peaked at $E_1$ and $E_2$ respectively. Two fit examples are shown in Fig. 3.4 for the BEGe dataset. The fit functions have parameters set to the global mode values calculated starting from the corresponding posterior marginalized distributions. The 68% uncertainty band was derived following the procedure illustrated in Ref. [22]. In particular, for a fixed energy $E_0$, a distribution of $M_0(E)$ or $M_1(E)$ values was produced at different $E$-values inside the fit window. The central 68% probability interval of the final $M_0(E)$ or $M_1(E)$ distributions defines the uncertainty band that is shown in the figure.

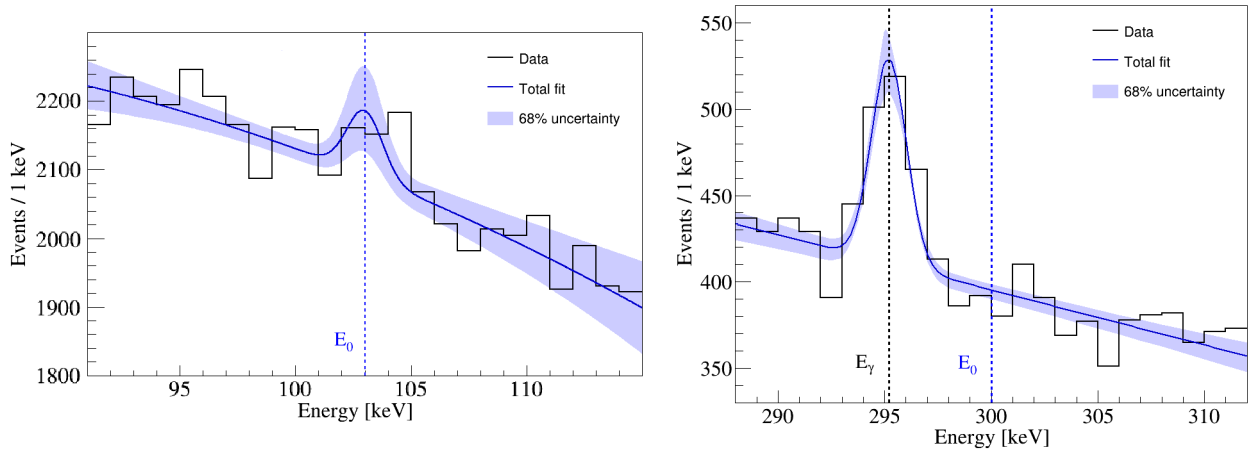


Figure 3.4: best fit (dark blue line) and 68% uncertainty (light blue band) for a signal at $E_0$ for the BEGe dataset. Left plot: fit for a signal expected at $E_0 = 103$ keV; a second-order polynomial is used for modelling the background; the signal excess is $2.1\bar{\sigma}$. Right plot: fit for a signal expected at $E_0 = 300$ keV; a first-order polynomial and a Gaussian at $E_\gamma = 295.224\,(2)$ keV are used for modelling the background.

| Origin | $T_{1/2}$ | Transition | Energy [keV] | BR [%] |
|---|---|---|---|---|
| $^{228}$Ac | 6.15 (3) h | $\gamma_{8,5}$ (Th) | 478.4 (5) | 0.224 (19) |
| | | $\gamma_{12,1}$ (Th) | 911.196 (6) | 26.2 (8) |
| | | $\gamma_{12,0}$ (Th) | 968.960 (9) | 15.9 (5) |
| $^{208}$Tl | 3.058 (6) min | $\gamma_{2,1}$ (Pb) | 583.187 (2) | 85.0 (3) |
| $^{212}$Pb | 10.64 (1) h | $\gamma_{2,0}$ (Bi) | 238.632 (2) | 43.6 (5) |
| $^{214}$Pb | 29.916 (44) min | $\gamma_{4,1}$ (Bi) | 241.997 (3) | 7.268 (22) |
| | | $\gamma_{4,0}$ (Bi) | 295.224 (2) | 18.414 (36) |
| | | $\gamma_{5,0}$ (Bi) | 351.932 (2) | 35.60 (7) |
| $^{214}$Bi | 19.8 (1) min | $\gamma_{1,0}$ (Po) | 609.312 (7) | 45.49 (19) |
| $^{85}$Kr | 10.752 (23) a | $\gamma_{2,0}$ (Rb) | 513.997 (5) | 0.435 (10) |
| $e^+e^-$ | | | 511.0 | |

Table 3.3: electromagnetic transitions having branching ratios above 0.1% and energies below 1 MeV. [3, 24]

The first part of the SuperWIMP analysis, then, is dedicated to the search for one or two of these $\gamma$ peaks that could lie near the fit-window edges. If one or two peaks are present, the fit range can be enlarged or shrinked to either include or exclude the peaks in order to avoid ill-behaved intermediate situations. In total, 23 cases for the position of one or two peaks with respect to the fit window were found. In extreme cases, the minimum size achieved for the fit window is 17 keV, while the maximum size is 31 keV. The general procedure applied to change the width of the fit window is the following one:

- the left and right edges of the fit window are increased by one FWHM if a gamma peak lies within 2 FWHM from one of the two edges, but the peak is inside the fit window; the peak, therefore, will be included in the fit function;
- the left and right edges of the fit window are decreased by one FWHM if a gamma peak lies within 2 FWHM from one of the two edges, but the peak is outside the fit window; the peak, therefore, will be excluded from the fit function;
- the left and right edges of the fit window are decreased by 1.5 FWHM if a gamma peak coincides exactly with the left or right edge of the window itself.

### 3.2.4 Fit Parameters

Taking into account the model fit functions (see Eq. (3.5) or (3.9)), one has to define a prior distribution for each of the parameters that enter into them. The position and smearing of the Gaussian functions are nuisance parameters that can be fixed knowing the energy at which the peak is centred and the energy dependence of the Germanium detectors resolution, respectively. Instead, for primary parameters of interest, i.e. the signal height or the background parameters, uniform prior distributions were adopted. Thus, for these parameters, it is necessary to specify the range into which each prior distribution function $P_0(\lambda)$ is different from zero, i.e. the range $[\lambda_{min}; \lambda_{max}]$ in which

$$P_0(\lambda) = \begin{cases} p_0, & \text{if } \lambda \in [\lambda_{min}; \lambda_{max}] \\ 0, & \text{otherwise} \end{cases} \tag{3.10}$$

where $p_0$ is a non-null value. As regards the range, the signal strength is defined into

$$\left[0; \mathrm{MAX}((R + 5\sqrt{B_S} + 5\sqrt{R}),\ 8\sqrt{B_S},\ 10)\right] \tag{3.11}$$

to provide a sufficiently wide range into which the parameter can vary. Here, $B_S$ and $R$ are respectively the background and signal contribution evaluated in the signal region, i.e. in the range $E_0 \pm 1.5$ FWHM.

These quantities are given by

$$B_S = \sum_{i=1}^{N_{sig}} B_{avg} \tag{3.12}$$

$$R = \sum_{i=1}^{N_{sig}} (R_i - B_{avg}) \tag{3.13}$$

where $N_{sig}$ and $R_i$ are the number of bins and entries in the signal region, while $B_{avg}$ is the average number of background events evaluated in the background region (see Fig. 3.5), which extends over $N_{bkg}$ bins:

$$B_{avg} = \frac{\sum_{j=1}^{N_{bkg}} B_j}{N_{bkg}} \tag{3.14}$$

Particular attention is paid when dealing with additional $\gamma$ peaks when evaluating the average background entries in the fit window: indeed, each Gaussian term must be carefully included since its presence could change the estimation of fit parameters.
Concerning the background lines, the prior distributions for the Gaussian heights are defined over a range equal to the one of Eq. (3.11), where the $\gamma$-signal region now becomes $E_\gamma \pm 1.5\,\mathrm{FWHM}$.

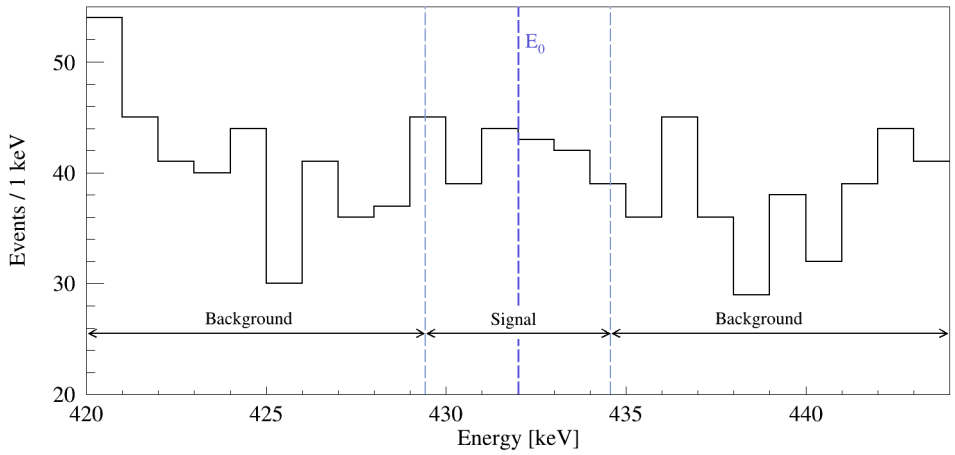


Figure 3.5: definition of the signal ($E_\gamma \pm 1.5\,\mathrm{FWHM}$) and background regions inside the fit window.

Since the Bayesian fit convergence is highly dependent on the range of the background polynomial parameters, the minimum and maximum allowed values for these parameters are defined starting from a preliminary fit done through the Minuit algorithm using the ROOT package in the range $E_0 \pm 20\,\mathrm{keV}$. The preliminary fit was done taking into consideration potential $\gamma$ peaks inside this range; in addition to these, the signal peak centred on $E_0$ is also included in the preliminary fit if the following condition is satisfied:

$$R > 3\sqrt{B_S} \tag{3.15}$$

i.e. if the signal height is sufficiently high with respect to expected background fluctuations. The values ($X$) and corresponding errors ($\sigma_X$) estimated in this way are then used to define the range inside which the background parameters have a non-null prior distribution; in particular, the range for these priors is chosen as $X \pm 10\,\sigma_X$. Nevertheless, these ranges, sometimes, are too tight, leading to truncated posterior marginalized distribution functions. In this case, the final quantiles of the posteriors are imprecisely estimated. To overcome this problem and to entirely contain the posteriors, the Bayesian fit was performed multiple times as a fit routine procedure until the first and last bins of the posterior marginalized distribution functions are empty. In particular, after each fit iteration, the range of the priors was enlarged. On average, acceptable results were obtained after four fit iterations at most or, even if more rarely, after an average of ten iterations at most.

## 3.3 Detection Efficiency

The total efficiency to observe a SuperWIMP absorption in the HPGe diodes is determined as:

$$\epsilon_{tot}(E) = \epsilon_{cut} \cdot \epsilon_{e^-}(E) \tag{3.16}$$

where $\epsilon_{cut}$ is the efficiency of the quality cuts and $\epsilon_{e^-}$ is the efficiency of the full energy absorption of the electron emitted after the SuperWIMP interaction (see Sec. 3.3.1). Since $\epsilon_{e^-}$ refers to the combined datasets and not to the individual detectors of each dataset, $\epsilon_{tot}$ refers to combined datasets too. The total detection efficiency varies with energy because of its dependence on the energy-dependent electron detection efficiency. Indeed, the electron released after a SuperWIMP interaction can partly deposit its energy on the $n^+$ electrode of a detector or lose its energy by emitting Bremsstrahlung radiation. Since the energy loss increases for higher and higher energies, one expects to observe a total detection efficiency that decreases for increasing energy values [3].
Quality cuts were applied to remove non-physical events by inspecting waveform parameters (e.g. baseline, leading edge, decay tail). In this way, events that only contain the baseline, test pulses or pile-ups (i.e. events for which there is an overlap between the waveforms of two consecutive events) were not included in the final energy spectra. For Phase II and Phase II+ data, the survival fraction of non-physical events is negligible ($\lesssim 1\%$), so $\epsilon_{cut}$ is taken as 100%. The efficiencies for muon veto and tagging only multiplicity-one events are taken as 100% too. Eq. (3.16) already takes into account the efficiency of the LAr cut through the electron detection efficiency. In particular, the LAr cut efficiency was estimated as 100% by comparing $\epsilon_{e^-}$ obtained when the LAr cut is applied to when it is not.
Fig. 3.6 and 3.7 show the total detection efficiency for Phase II and Phase II+, respectively. In Tab. 3.4, total efficiencies are reported for each dataset at 60 keV (analysis' start point) and 1000 keV (analysis' end point) for Phase II and Phase II+.

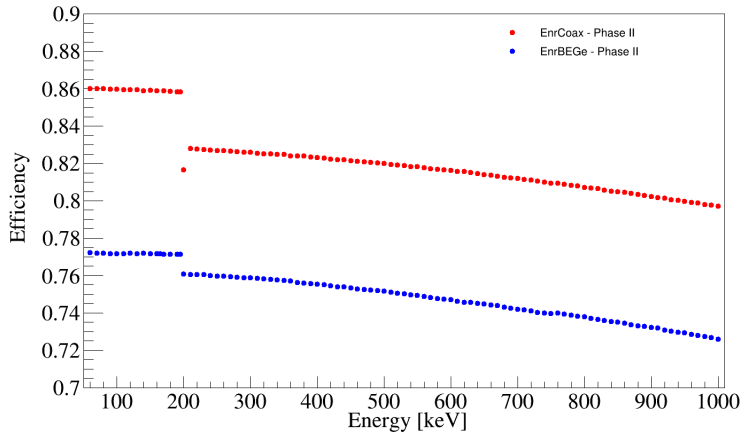


Figure 3.6: Phase II total detection efficiencies for enriched coaxial (red) and BEGe (blue) detectors. Values below the energy threshold at 195 keV refer to data collected after October 2017 (run $87 - 93$).

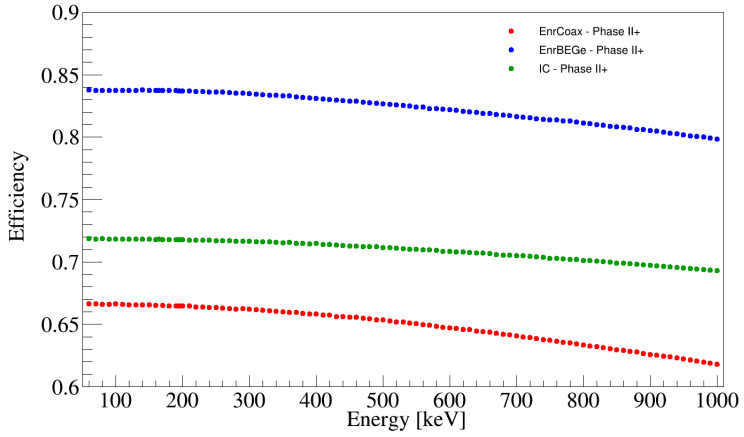


Figure 3.7: Phase II+ total detection efficiencies for enriched coaxial (red), BEGe (blue) and IC (green) detectors.

| Detector | Phase | $\epsilon_{tot}$(60 keV) | $\epsilon_{tot}$(1000 keV) |
|---|---|---|---|
| Coaxial | II | 86.01 % | 79.71 % |
| | II+ | 66.65 % | 61.80 % |
| BEGe | II | 77.21 % | 72.59 % |
| | II+ | 83.77 % | 79.86 % |
| IC | II+ | 71.87 % | 69.30 % |

Table 3.4: total detection efficiencies at 60 keV (analysis' start point) and 1000 keV (analysis' end point) for each dataset for Phase II and Phase II+.

In Fig. 3.6, there is a jump around 200 keV caused by the difference in exposure for energies below and above this energy threshold. Moreover, coaxial Phase II efficiencies turned out to be higher than coaxial Phase II+ efficiencies, and vice versa for the BEGe efficiencies. This difference is primarily related to detectors' on and off times. For instance, BEGe efficiencies are worse in Phase II due to the presence of three non-operating detectors, which are the GD91C, GD02D and GD91B. Indeed, the first detector had a broken JFET [19], while the other two could be used only in AC mode.

### 3.3.1 Electron Detection Efficiency

The electron detection efficiencies were estimated for each detector dataset using the MAjorana-GErda (MaGe) framework by performing a Monte Carlo simulation of $10^7$ uniformly distributed electrons in the detectors' volume, active or dead. Off detectors were already included in the simulations, as well as the detectors' weighting by exposure. See Tab. 4.2 and 4.3 of Appendix B for detectors' mass and exposure values used in the simulations.
Monte Carlo simulations were performed every 10 keV inside the range $[60; 1000]$ keV, separately for Phase II and Phase II+ data. In Fig. 3.8, the energy distribution of events having initial energy of 900 keV is shown as an example. The electron energy is not entirely deposited around the initial energy value since a continuous distribution of events is also present at lower energies.

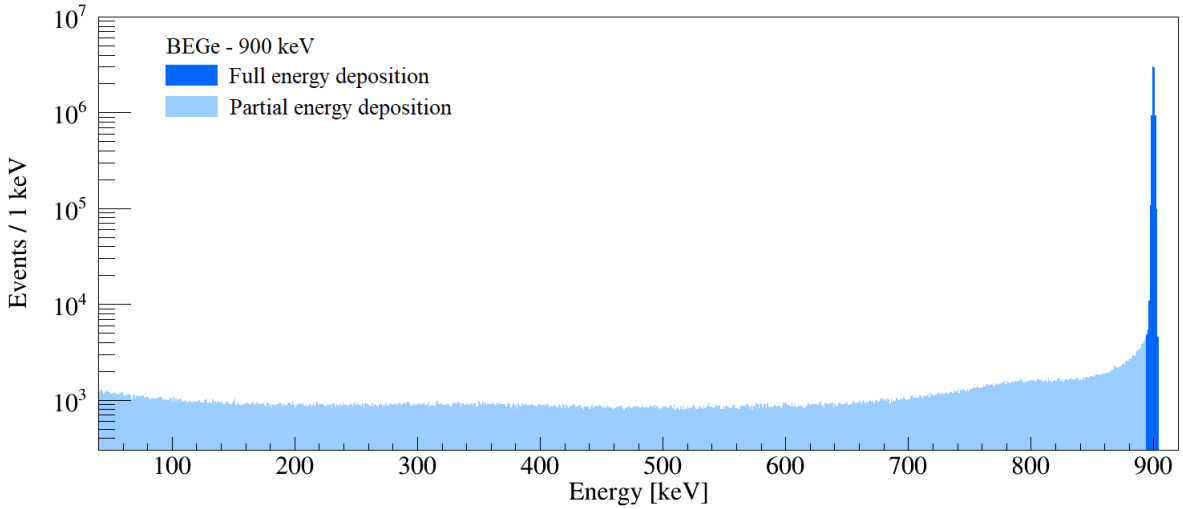


Figure 3.8: energy distribution of LAr vetoed events having initial energy of 900 keV and multiplicity equal to one (BEGe dataset). Light blue: energy loss due to Bremsstrahlung radiation. Dark blue: full energy loss inside BEGe detectors.

For fixed initial energy $\bar{E}$, the electron detection efficiency is computed as the ratio between the number of entries that released the whole initial energy inside the detector and the total number of electrons initially produced in the Germanium detectors' volume ($N_{tot} = 10^7$):

$$\epsilon_{e^-}(\bar{E}) = \frac{\int_{E_{min}}^{E_{max}} N(E)\, dE}{N_{tot}} \,. \tag{3.17}$$

Starting from the energy distribution of events, $[E_{min}; E_{max}]$ is the signal region, chosen to be about $5\sigma$ wide (where $\sigma$ is the detectors' resolution, see Eq. (3.6)). Thus, the signal region is defined to entirely include the full energy peak centred on $\bar{E}$.
Since efficiencies are not known keV by keV in the energy range $[60; 1000]$ keV, for electrons having energies different from the simulated ones, the efficiency was calculated by extrapolation. In particular, we considered a linear function of the type

$$\epsilon_{e^-}(E) = p_0 + p_1 \cdot E \tag{3.18}$$

between two consecutive electron detection efficiencies evaluated at energies included in the simulations.

# Chapter 4

# Analysis Results

## 4.1 Signal Counting Rate Limits

In Fig. 4.1, the estimated 90% C.I. upper limits for the signal counting rate are shown for each type of detector after being normalized by the exposure (see Tab. 3.1). For each dataset, upper limits increase more and more when going from right towards the energy threshold at 195 keV. This increase is caused by the presence of the $^{39}$Ar $\beta^-$ decay, which is characterized by an end-point energy of 565 keV [20]. In particular, the presence of $^{39}$Ar is more visible in the enriched coaxial dataset because of the higher amount of $\beta^-$ decay events that were collected by the coaxial detectors (see Fig. 3.2). The 90% C.I. upper limit distributions are characterized by many fluctuations, but most of them are solely related to the fluctuations already present in the physics energy spectra. Nevertheless, considering the procedure illustrated in Sec. 3.2.2, some excesses were found for BEGe detectors, but near known $\gamma$ lines. In Tab. 4.1, the energies $E_0$ for which a signal excess was observed are listed; in Fig. 4.11 of Appendix A, the corresponding Bayesian fits are shown. For these energies, 90% C.I. upper limits were set irrespective of the signal counting rate mode. The observation of excesses near known $\gamma$ lines is likely related to deviations of the peak shapes from the ones used in the fit functions, especially in the case of peaks having high branching ratios.

| $E_0$ [keV] | Mode [cts/kg·yr] | Mode/$\bar{\sigma}$ | $\gamma$ origin |
|---|---|---|---|
| 238 | $8.5^{+0.3}_{-2.3}$ | 6.5 | $^{212}$Pb, $^{214}$Pb |
| 350 | $3.2^{+0.6}_{-0.6}$ | 5.2 | $^{214}$Pb |
| 351 | $4.7^{+0.8}_{-0.8}$ | 5.8 | |

Table 4.1: list of energies for which a signal excess was observed for BEGe detectors. The global mode, with uncertainties estimated from the $L_{68}$ and $U_{68}$ quantiles, and the mode to $\bar{\sigma}$ ratio are shown together with the $\gamma$ line to which the excess can be attributed.

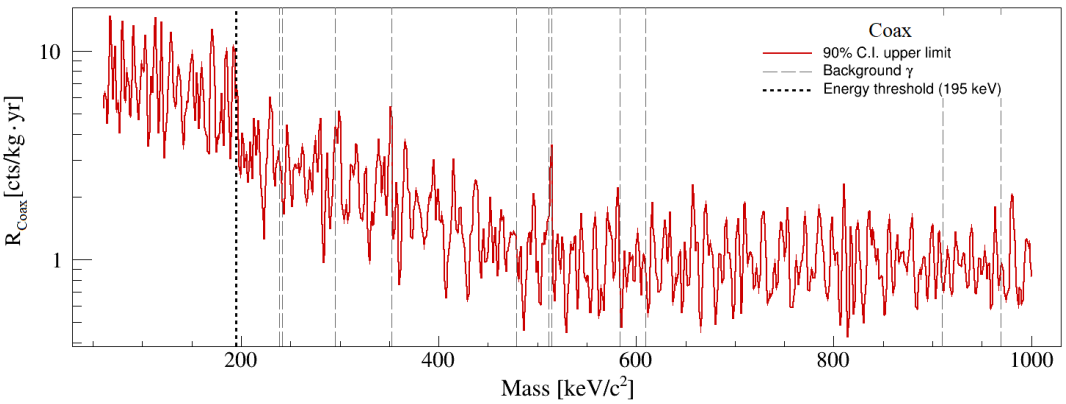

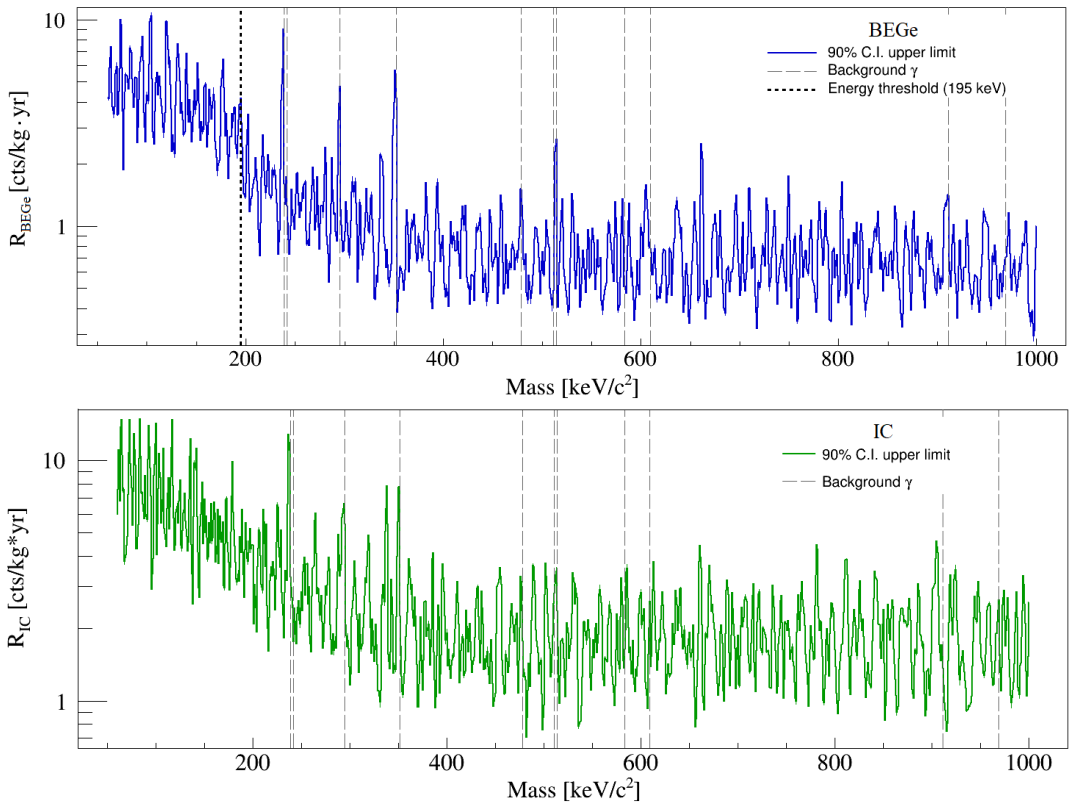


Figure 4.1: 90% C.I. upper limits for the signal counting rate estimated for enriched coaxial (top), BEGe (centre) and IC (bottom) detectors. Known $\gamma$ lines are shown with dashed, gray lines; the energy threshold at 195 keV is also shown for coaxial and BEGe datasets.

In Fig. 4.2, the frequency for the ratio of the global modes with respect to the error (defined by Eq. (3.3) or (3.4)) is shown for each dataset. In general, there is a high frequency that the global mode of the signal counting rate is compatible with zero counts.
In Fig. 4.3 and 4.4, the background parameters, i.e. the offset, the slope and the curvature parameters that enter into Eq. (3.7) and (3.8), are shown for each type of detector. For coaxial and BEGe datasets, there is a gap at around 195 keV related to different amounts of statistics collected below and above the threshold. For IC detectors, the gap is not visible because of the absence of the threshold in the energy spectrum. Since the modelling of the continuous background below 195 keV requires a second-order polynomial, the curvature parameter is non-null up to 195 keV.

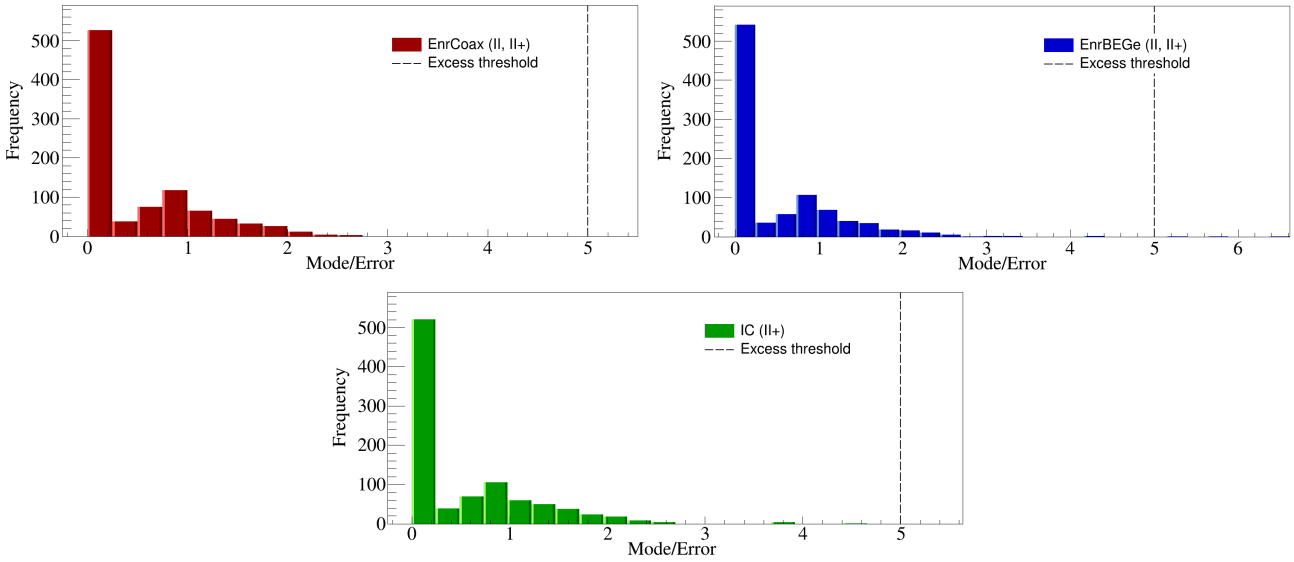


Figure 4.2: frequency of mode to error ratios for coaxial (top left), BEGe (top right) and IC (bottom) datasets; errors are calculated using Eq. (3.3) or (3.4). The excess threshold is shown in black.

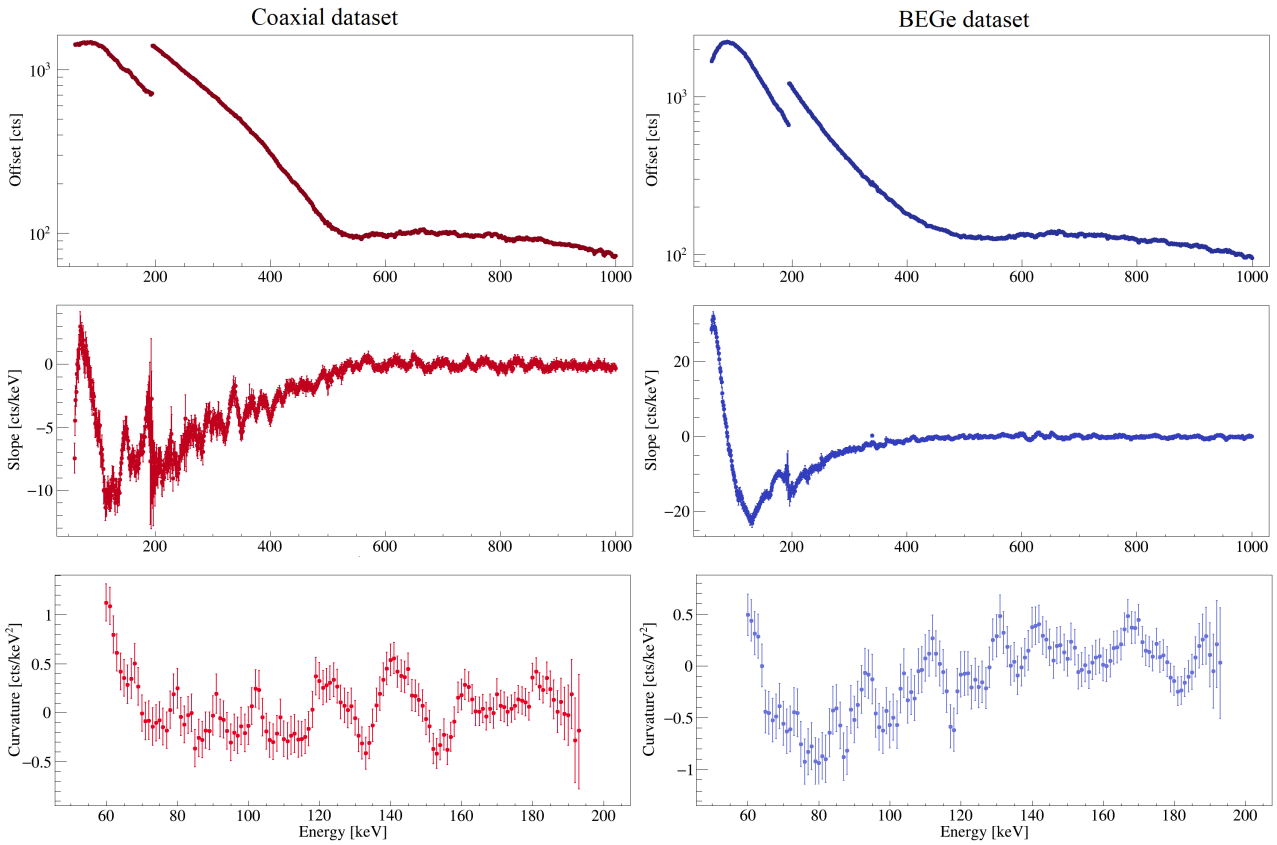


Figure 4.3: global mode and 68% central interval for the background parameters (left: coaxial dataset; right: BEGe dataset).

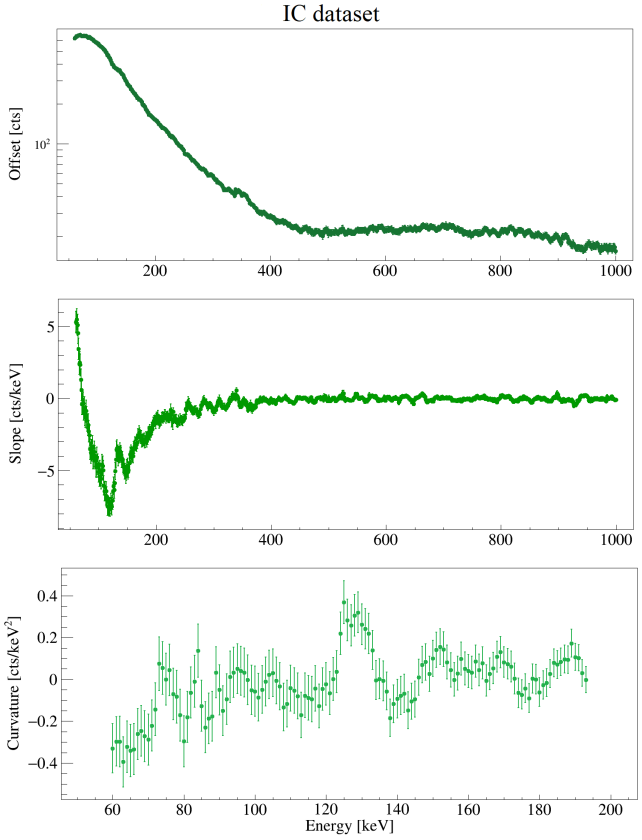


Figure 4.4: global mode and 68% central interval for the background parameters for IC detectors.

## 4.2 Monte Carlo Study of the Analysis Procedure

To understand better the fit results, i.e. the behaviour of the 90% C.I. upper limits for the signal counting rate, toy Monte Carlo spectra were generated and then analyzed following the fit procedure described in Section 3.2. Assuming Poisson fluctuations for bin contents, spectra were generated for each energy by sampling the background parameters from the posterior marginalized distributions obtained with the Bayesian analysis when applied to real data. From each simulated spectrum, the 90% C.I. upper limit was derived after having considered a model function given by the sum of the background and the signal (see Eq. (3.5) and (3.9)). Then, after $\mathcal{O}(500)$ simulations, a distribution of upper limits was created for the under-study value of energy (see Fig. 4.5). From this distribution, the median value together with the $1\sigma$ (68.3%), $2\sigma$ (95.5%) and $3\sigma$ (99.7%) probability bands were calculated. In particular, the median shows the value that one expects to observe in case of no signal over the background.
For reasons of time, only two regions of the BEGe spectrum were considered. The analyzed ranges are:

- $[289; 302]$ keV to investigate the Bayesian analysis output when there is one $\gamma$ peak;
- $[502; 523]$ keV to investigate the Bayesian analysis output when there are two $\gamma$ peaks.

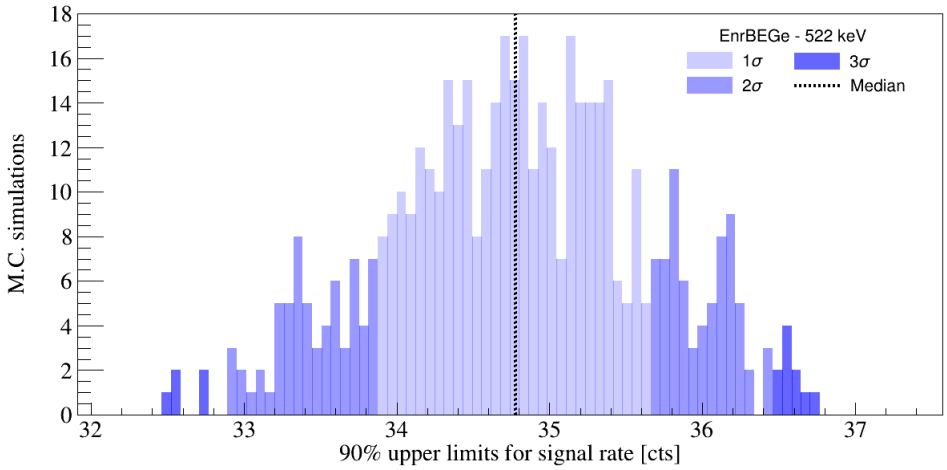


Figure 4.5: 90% upper limit distribution for signal counting rate for $E_0 = 522$ keV (BEGe dataset). The black dotted line represents the median value.

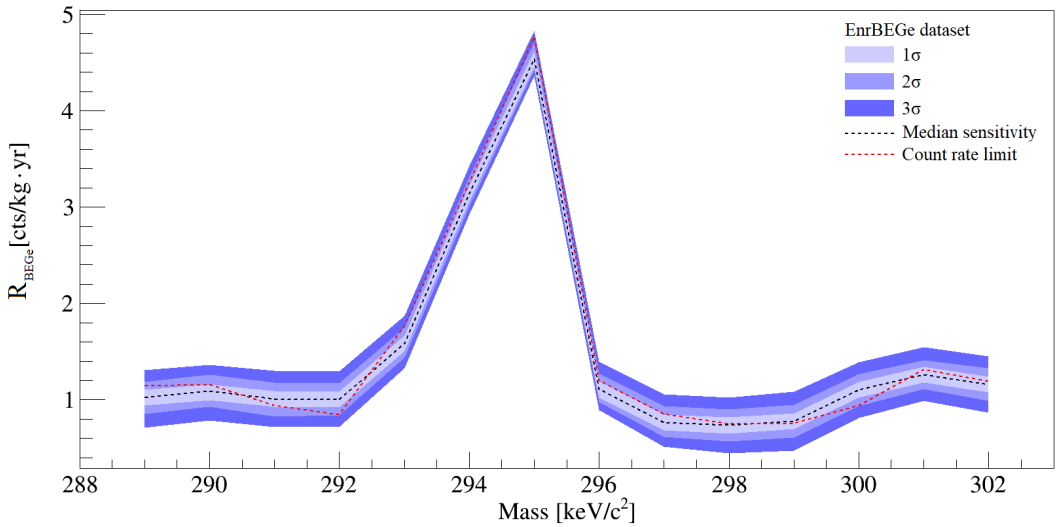


Figure 4.6: estimated 90% C.I. upper limits (red line), expected median (black line) and exclusion bands for BEGe detectors inside the $[289; 302]$ keV energy range. In this energy window, there is one $\gamma$ peak centred on $E_\gamma = 295.224\,(2)$ keV.

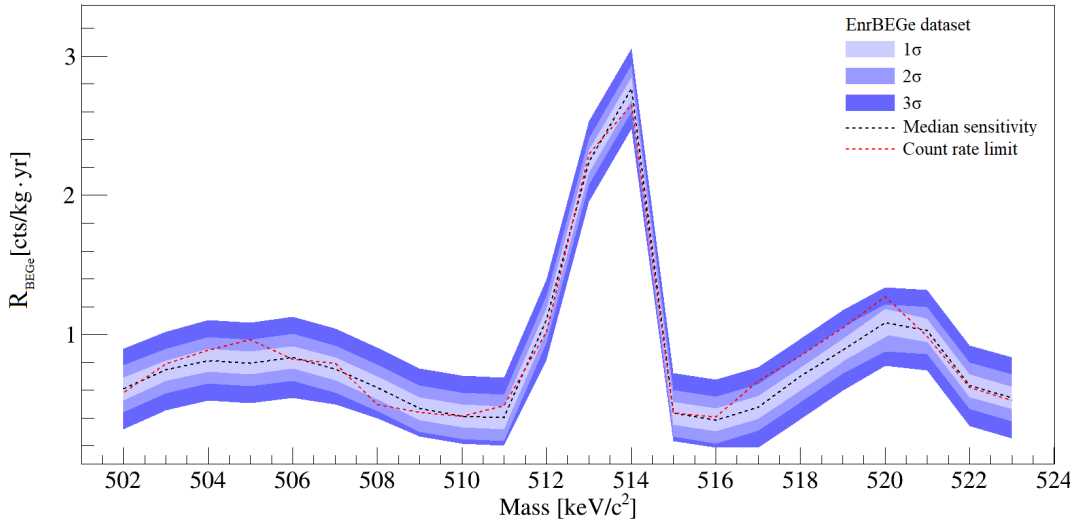


Figure 4.7: estimated 90% C.I. upper limits (red line), expected median (black line) and exclusion bands for BEGe detectors inside the [502; 523] keV energy range. In this energy window, there are two $\gamma$ peaks centred on $E^1_\gamma = 511$ keV and $E^2_\gamma = 513.997\,(5)$ keV.

In Fig. 4.6 and 4.7, the estimated 90% C.I. upper limits for the signal counting rate (see Fig. 4.1) are displayed together with the Monte Carlo results for the signal's count rate of BEGe detectors inside the [289; 302] and [502; 523] keV energy ranges.
Close to the expected electromagnetic transitions, the exclusion sensitivity increases together with the estimated upper limits, reflecting the presence of the background source. In particular, both values are higher for larger branching ratios. Instead, on the right and left of the expected $\gamma$ lines, values tend to fluctuate with respect to the estimated median sensitivity because of background fluctuations. In general, no cases where the limit exceeds the $3\sigma$ band are present in the two analyzed energy ranges.
This preliminary study helps to understand the model behaviour while searching for signals that are not compatible with known background sources. One expects to find similar results for the remaining energies inside the [60; 1000] keV energy range, as demonstrated for coaxial and BEGe detectors in Ref. [25] for Phase II data only.

## 4.3 SuperWIMP Coupling Strengths

Starting from Eq. (1.10) and (1.11), one can derive the expression for pseudoscalar ($g_{ae}$) and vector ($\alpha'/\alpha$) dimensionless coupling strengths of SuperWIMPs to electrons respectively as follows:

$$g_{ae} \approx \sqrt{\frac{A \cdot R_{ALP}}{1.29 \cdot 10^{19}} \left(\frac{[\mathrm{keV/c^2}]}{m_a}\right) \left(\frac{[b]}{\sigma_{pe}}\right) [kg \cdot d]} \tag{4.1}$$

$$\frac{\alpha'}{\alpha} \approx \frac{A \cdot R_{DP}}{4 \cdot 10^{23}} \left(\frac{m_{\gamma'}}{[\mathrm{keV/c^2}]}\right) \left(\frac{[b]}{\sigma_{pe}}\right) [kg \cdot d] \tag{4.2}$$

where $A = 76$ for Germanium detectors enriched in the $^{76}$Ge isotope. The absorption rates of SuperWIMPs in Germanium detectors, i.e. $R_{ALP}$ and $R_{DP}$, are taken as 90% upper limits for the signal counting rate (see Fig. 4.1) defined as the number of counts divided by the exposure (which is different depending on the SuperWIMP mass at which coupling strengths are evaluated, see 3.1). For the signal counting rate, one must also account for the total detection efficiency calculated in Sec. 3.3.
In Eq. (4.1) and (4.2), SuperWIMP masses $m_a$ and $m_{\gamma'}$ are taken equal to the energy since these particles belong to the cold sector of DM, for which kinetic energies are small.
As regards $\sigma_{pe}$, i.e. the total Germanium photoelectric absorption cross section (see Fig. 4.8), values were derived keV by keV in the [60; 1000] keV energy range from Ref. [26].

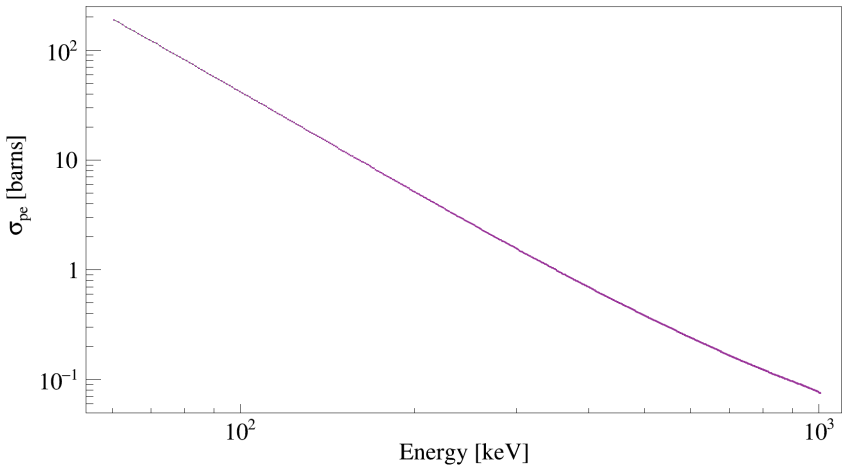


Figure 4.8: total photoelectric absorption cross section $\sigma_{pe}$ on Germanium in the [60; 1000] keV energy range. Values decrease with energy, starting from about $\sigma_{pe} = 214$ b at 60 keV down to $\sigma_{pe} = 0.086$ b at 1 MeV.

The combined upper limits for SuperWIMP coupling strengths to electrons were estimated weighing each dataset by its exposure:

$$R_{tot} = \frac{R_{coax} \cdot \xi_{coax} + R_{BEGe} \cdot \xi_{BEGe} + R_{IC} \cdot \xi_{IC}}{\xi_{coax} + \xi_{BEGe} + \xi_{IC}} \tag{4.3}$$

where $R_D$ and $\xi_D$ are respectively the signal counting rate and the exposure for a given dataset $D$[1]. As an example, at a mass of 1 MeV/c$^2$, the old analysis set direct limits on the dimensionless couplings of $g_{ae} < 1.1 \times 10^{-11}$ and of $\alpha'/\alpha < 3.5 \times 10^{-21}$ for pseudoscalar and vector SuperWIMPs, respectively [3]. The analysis was performed on Phase II data only, namely on events collected between December 2015 and April 2018. Instead, the thesis work focused on a larger dataset given by the combination of Phase II and Phase II+ (July 2018−November 2019) data. In this case, we set direct limits on the dimensionless couplings of $g_{ae} < 5.2 \times 10^{-12}$ and of $\alpha'/\alpha < 8.7 \times 10^{-22}$ for pseudoscalar and vector SuperWIMPs, respectively. The overall improvement obtained for the coupling strength limits with respect to previous results is due to having used more statistics for the analysis. Fig. 4.10 displays the old and new results obtained with data collected by GERDA.

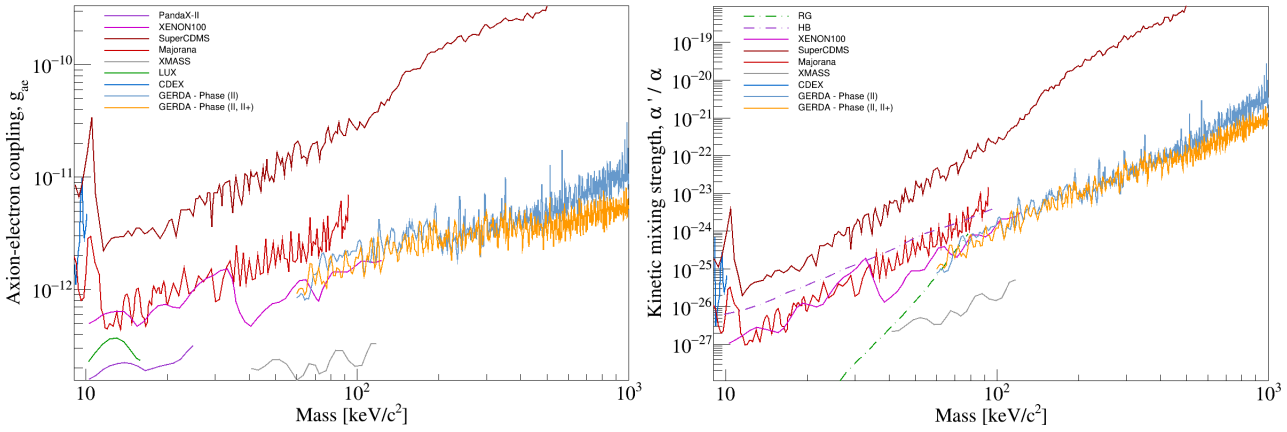


Figure 4.9: dimensionless coupling strengths to electrons for pseudoscalar (left) and vector (right) SuperWIMPs. Upper limits were derived by combining the 90% C.I. upper limits obtained for each type of detector using Eq. (4.3). Old results are labelled as "GERDA - Phase (II)", while results from the current work are labelled as "GERDA - Phase (II, II+)".

[1] Actually, Eq. (4.3) is not statistically correct. To combine the results of each dataset, the right procedure consists in performing a combined fit. For instance, using flat priors for the signal counting rate, one could start by applying the Bayesian analysis to the coaxial dataset. Once the posteriors are obtained, these distributions should be used as priors for the fit of the BEGe dataset. Then, BEGe posteriors should be used as priors for the signal counting rate when performing the fit of the IC datasets. Eventually, the final results should be employed to evaluate the combined coupling strengths of super-WIMPs. This analysis procedure was not pursued for reasons of time.

The novelty of this analysis performed with data collected by GERDA consisted of extending the SuperWIMP search region up to 1 MeV. As in the previous analysis, GERDA put the best constraints for mass in the $[120; 1000]$ keV/c$^2$ range with respect to other direct and indirect searches, while for mass below 120 keV/c$^2$ GERDA results are compatible with other direct searches, like XENON100. Coupling strength limits display multiple peaks and fluctuations related to the behaviour of 90% C.I. upper limits for the signal counting rates. Fluctuations were proved to be related only to background fluctuations or to the presence of $\gamma$ lines, especially when these electromagnetic transitions have high branching ratios. Notice that pseudoscalar and vector SuperWIMP coupling strengths space over $1-4$ orders of magnitude because of their dependence on the Germanium photoelectric absorption cross section, which varies of about 4 orders of magnitude going from 60 keV to 1 MeV (see Fig. 4.8).

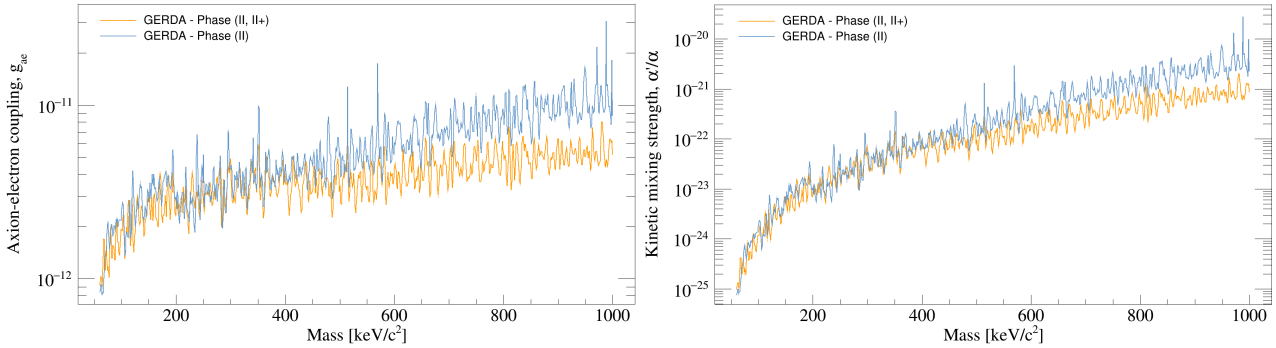


Figure 4.10: upper limits for dimensionless coupling strengths for pseudoscalar (left) and vector (right) SuperWIMPs. Old results, which combine only Phase II data for coaxial and BEGe datasets, are shown in blue; new results are shown in orange.

# Summary and Conclusions

In this thesis work, we performed a generic peak search in the energy spectrum consisting of data collected by GERDA from December 2015 to November 2019. The search for an unexpected signal over the background could be explained by the presence of new physics, e.g. SuperWIMPs. Thus, applying a binned Bayesian analysis to events collected by GERDA in the $[60; 1000]$ keV energy range, 90% C.I. upper limits were derived for pseudoscalar and vector SuperWIMP coupling strengths to electrons.

The analysis proved there are no signals over the background. The only signal excesses found were in the BEGe dataset, but they are justified by the presence of nearby $\gamma$ lines. Indeed, since those signal excesses lie within $5\sigma$ from known electromagnetic transitions (where $\sigma$ is the detector's resolution), 90% C.I. upper limits for the signal counting rate were set irrespective of the global mode of the corresponding posterior marginalized distribution function.
Through the absorption rate formula of SuperWIMPs inside Germanium Earth-bound detectors, we converted the 90% C.I. upper limits for the signal counting rate into 90% C.I. upper limits for the pseudoscalar ($g_{ae}$) and vector ($\alpha'/\alpha$) SuperWIMP coupling strengths to electrons. Comparing the new results to the old ones (see Ref. [3]), we noticed that limits improved for most of the energies in the $[60; 1000]$ keV/c$^2$ mass range. In particular, at a mass of 1 MeV/c$^2$, limits at 90% C.I. of $g_{ae} < 1.1 \times 10^{-11}$ and $\alpha'/\alpha < 3.5 \times 10^{-21}$ were obtained in the previous analysis, while in the current work we set limits at 90% C.I. of $g_{ae} < 5.2 \times 10^{-12}$ and $\alpha'/\alpha < 8.7 \times 10^{-22}$. This improvement can be explained by the fact that more statistic was available for the analysis we performed. In particular, BEGe (coaxial) detectors collected about 22.9 (13.8) kg·yr of exposure more in the $[60; 195]$ keV energy range and approximately 24.1 (13.7) kg·yr of exposure more in the $[195; 5200]$ keV energy range; moreover, additional 8.8 kg·yr of exposure were available over the whole energy range thanks to the employment of 5 new IC detectors after the GERDA upgrade in 2018.

To summarize, the novelty of GERDA with respect to other direct and indirect searches for keV-DM candidates consisted in extending the analyzed mass region up to 1 MeV/c$^2$, setting the best constraints among all other experiments for masses above 120 keV/c$^2$. Moreover, through this analysis, we demonstrated the capability of GERDA to search for other rare phenomena besides the $^{76}$Ge neutrinoless double-beta decay. This type of study will be helpful for the understanding of events characterized by energies below 1 MeV, which can be further interpreted in terms of other new physics.
In the future, the direct limits set for SuperWIMP coupling strengths may be improved in two ways. First, one can apply PSD cuts to events. Indeed, studying the time dependence of the detector's current pulses, one can select only those single-site events compatible with a SuperWIMP interaction inside one Germanium detector. Since PSD cuts are crucial for the $0\nu2\beta$ analysis, the application of PSD cuts at energies in the $[60; 1000]$ keV energy range is still under study. Secondly, a second SuperWIMP interaction process can be included in the total cross section. Indeed, a SuperWIMP can also interact with an electron, releasing a photon in the final state through the so-called Compton-like process. In Ref. [27], they obtained that the cross section for this additional process is higher than the absorption cross section for mass above approximately 150 keV/c$^2$ for both pseudoscalar and vector super-WIMPs. In particular, they found that $\sigma_{cmp,\,ALP} \sim 10 \cdot \sigma_{abs,\,ALP}$ at 1 MeV/c$^2$ for pseudoscalar SuperWIMPs and $\sigma_{cmp,\,DP} \sim 10^2 \cdot \sigma_{abs,\,DP}$ at 1 MeV/c$^2$ for vector SuperWIMPs. The inclusion of this second process in the total cross section could improve the experimental upper limits.

Finally, better upper limits will be obtained in the future thanks to LEGEND-200 (Large Enriched Germanium Experiment for Neutrinoless $\beta\beta$ Decay), an experiment whose commissioning will start in Fall 2021. LEGEND-200 is planned to operate 200 kg of Germanium detectors in a lower background regime, namely approximately five times lower than what was achieved at GERDA. Thus, the sensitivity to new physics will be improved in LEGEND-200 thanks to the lower background rate and the employment of more Germanium. Moreover, the energy threshold will be further lowered, allowing to extend the generic peak search analysis down to approximately 1 keV.

# Appendix A

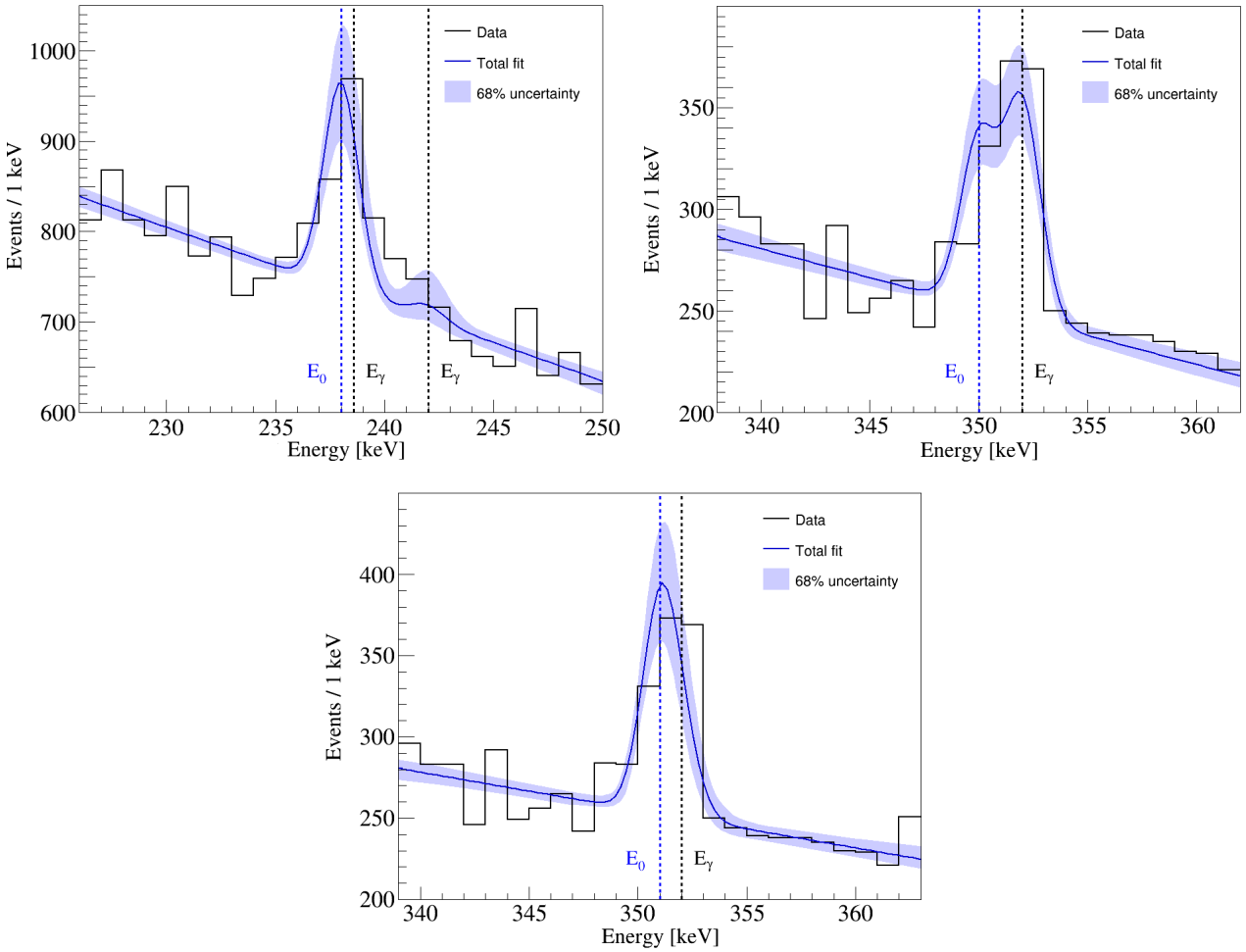


Figure 4.11: best fit (dark blue line) and 68% uncertainty (light blue band) for a signal at $E_0$ for the BEGe dataset. The figures correspond to energies displayed in Tab. 4.1 for which a signal excess was found. In the end, the excesses can be traced back to the presence of known $\gamma$ lines.
Top left plot: $E_0 = 238$ keV ($E_\gamma = 238.632\,(2)$ keV, $E_\gamma = 241.9971\,(3)$ keV). Top right plot: $E_0 = 350$ keV ($E_\gamma = 351.9321\,(2)$ keV). Bottom plot: $E_0 = 351$ keV ($E_\gamma = 351.9321\,(2)$ keV).

# Appendix B

| Detector | Channel | $M_{tot}$ [g] | $M_{av}$ [g] | $\xi$ [kg · yr] |
|---|---|---|---|---|
| GD91A | 0 | 627.00 | 5571 (11) | 1.93 |
| GD35B | 1 | 810.00 | 740 (12) | 2.49 |
| GD02B | 2 | 625.00 | 553 (11) | 1.92 |
| GD00B | 3 | 697.00 | 613 (13) | 2.08 |
| GD61A | 4 | 731.00 | 652 (13) | 2.24 |
| GD89B | 5 | 620.00 | 533 (13) | 1.41 |
| GD02D † | 6 | 662.00 | 552 (11) | 0.00 |
| GD91C | 7 | 626.00 | 556 (12) | 0.99 |
| ANG5 | 8 | 2746.00 | 2281 (132) | 5.07 |
| RG1 | 9 | 2110.00 | 1908 (125) | 6.31 |
| ANG3 | 10 | 2391.00 | 2070 (136) | 7.27 |
| GD02A | 11 | 545.00 | 488 (9) | 1.68 |
| GD32B | 12 | 716.00 | 632 (11) | 2.14 |
| GD32A | 13 | 458.00 | 404 (11) | 1.04 |
| GD32C | 14 | 743.00 | 665 (11) | 2.29 |
| GD89C | 15 | 595.00 | 520 (13) | 1.79 |
| GD61C | 16 | 634.00 | 562 (11) | 1.87 |
| GD76B | 17 | 384.00 | 326 (8) | 1.18 |
| GD00C | 18 | 815.00 | 727 (15) | 2.47 |
| GD35C | 19 | 634.00 | 572 (10) | 1.95 |
| GD76C | 20 | 824.00 | 723 (13) | 2.54 |
| GD89D | 21 | 526.00 | 454 (10) | 1.62 |
| GD00D | 22 | 813.00 | 723 (14) | 2.50 |
| GD79C | 23 | 812.00 | 713 (12) | 2.20 |
| GD35A | 24 | 768.00 | 693 (13) | 2.37 |
| GD91B | 25 | 650.00 | 578 (11) | 1.25 |
| GD61B | 26 | 751.00 | 666 (13) | 2.04 |
| ANG2 | 27 | 2833.00 | 2468 (145) | 7.50 |
| RG2 | 28 | 2166.00 | 1800 (115) | 6.56 |
| ANG4 | 29 | 2372.00 | 2136 (135) | 7.30 |
| GD00A | 30 | 496.00 | 439 (9) | 1.53 |
| GD02C | 31 | 788.00 | 700 (14) | 2.39 |
| GD79B | 32 | 736.00 | 648 (14) | 1.36 |
| GD91D | 33 | 693.00 | 615 (13) | 1.99 |
| GD32D | 34 | 720.00 | 657 (11) | 2.07 |
| GD89A | 35 | 524.00 | 462 (10) | 1.61 |
| ANG1* | 36 | 958.00 | 795 (50) | 1.81 |
| GTF112 † | 37 | 2965.00 | 2522 (0) | 0.00 |
| GTF32 † | 38 | 2321.00 | 2251 (116) | 0.00 |
| GTF45_2 † | 39 | 2312.00 | 1965 (0) | 0.00 |

Table 4.2: summary of channel, total and active mass [19], and single exposure ($\xi = M_{tot} \cdot t$) for BEGe and coaxial detectors employed during the GERDA Phase II and II+. Detectors with an asterisk were used only during Phase II. Detectors with a dagger were not considered in the analysis. In the table, horizontal lines are used to distinguish detectors belonging to different strings.

| **Detector** | **Channel** | $\mathbf{M_{tot}}$ **[g]** | $\mathbf{M_{av}}$ **[g]** | $\boldsymbol{\xi}$ **[kg · yr]** |
|---|---|---|---|---|
| IC48B † | 36 | 1815.8 | 1698 (8) | 0.00 |
| IC50B | 37 | 1928.7 | 1809 (9) | 2.26 |
| IC48A | 38 | 1918.9 | 1796 (11) | 2.25 |
| IC50A | 39 | 1881.1 | 1731 (13) | 1.83 |
| IC74A | 40 | 2072.9 | 1893 (13) | 2.43 |

Table 4.3: summary of channel, total and active mass [28, 29], and single exposure ($\xi = M_{tot} \cdot t$) for IC detectors employed during the GERDA Phase II+. Detectors with a dagger do not contribute to the analysis. In the table, horizontal lines are used to distinguish detectors belonging to different strings.

# List of Acronyms

| | |
|---|---|
| **AC** | Anti-Coincidence |
| **ALP** | Axion-Like Particle |
| **BAT** | Bayesian Analysis Toolkit |
| **BEGe** | Broad Energy GErmanium |
| **BI** | Background Index |
| **CDM** | Cold Dark Matter |
| **C.I.** | Credible Interval |
| **DM** | Dark Matter |
| **DP** | Dark Photon |
| **DS** | Dark Sector |
| **FWHM** | Full Width at Half Maximum |
| **GERDA** | GERmanium Detector Array |
| **HDM** | Hot Dark Matter |
| **HPGe** | High Purity Germanium |
| **IC** | Inverted Coaxial |
| **INFN** | Istituto Nazionale di Fisica Nucleare |
| **LAr** | Liquid Argon |
| **LEGEND** | Large Enriched Germanium Experiment for Neutrinoless $\beta\beta$ Decay |
| **LNGS** | Laboratori Nazionali del Gran Sasso |
| **MaGe** | MAjorana-GErda |
| **MCMC** | Markov Chain Monte Carlo |
| **MS** | Mini-Shroud |
| **PSD** | Pulse Shape Discrimination |
| **PMT** | Photo-Multiplier Tube |
| **SiPM** | Silicon Photo-Multiplier |
| **SM** | Standard Model |
| **WIMP** | Weakly Interacting Massive Particles |
| **$0\nu2\beta$** | Neutrinoless double-beta decay |
| **$2\nu2\beta$** | Double-beta decay |

# Bibliography


[1] V. A. Mitsou, "Dark matter: experimental and observational status", arXiv: 1903.11589 (2019).

[2] C. Pérez de los Heros, "Status of direct and indirect dark matter searches", arXiv: 2001.06193 (2020).

[3] M. Agostini *et al.* (GERDA Collab.), "First Search for Bosonic Superweakly Interacting Massive Particles with Masses up to 1 MeV/$c^2$ with GERDA", Phys. Rev. Lett. **125**, 011801 (2020).

[4] B. J. Carr, "Baryonic and Non-Baryonic Dark Matter", arXiv: gr-qc/0008005 (1999).

[5] J. A. R. Cembranos and M. Kaplinghat, "Whitepaper on Super-weakly Interacting Massive Particles for Snowmass 2013", (2013).

[6] M. Pospelov, A. Ritz, and M. Voloshin, "Bosonic super-WIMPs as keV-scale dark matter", Phys. Rev. D **78**, 115012 (2008).

[7] E. Izaguirre and I. Yavin, "New window to millicharged particles at the LHC", Phys. Rev. D **92**, 035014 (2015).

[8] N. Blinov *et al.*, "Dark matter targets for axionlike particle searches", Phys. Rev. D **100**, 015049 (2019).

[9] T. Hambye *et al.*, "Dark matter from dark photons: A taxonomy of dark matter production", Phys. Rev. D **100**, 095018 (2019).

[10] E. Armengaud *et al.* (EDELWEISS Collab.), "Searches for electron interactions induced by new physics in the EDELWEISS-III germanium bolometers", Phys. Rev. D **98**, 082004 (2018).

[11] N. Abgrall *et al.* (Majorana Collab.), "New Limits on Bosonic Dark Matter, Solar Axions, Pauli Exclusion Principle Violation, and Electron Decay from the Majorana Demonstrator", Phys. Rev. Lett. **118**, 161801 (2017).

[12] T. Aralis *et al.* (SuperCDMS Collab.), "Constraints on dark photons and axionlike particles from the SuperCDMS Soudan experiment", Phys. Rev. D **101**, 052008 (2020).

[13] S. K. Liu *et al.* (CDEX Collab.), "Constraints on Axion couplings from the CDEX-1 experiment at the China Jinping Underground Laboratory", Phys. Rev. D **95**, 052006 (2017).

[14] C. Fu *et al.* (PandaX-II Collab.), "Limits on Axion Couplings from the First 80 Days of Data of the PandaX-II Experiment", Phys. Rev. Lett. **119**, 181806 (2017).

[15] E. Aprile *et al.* (XENON100 Collab.), "Search for bosonic super-WIMP interactions with the XENON100 experiment", Phys. Rev. D **96**, 122002 (2017).

[16] D. S. Akerib *et al.* (LUX Collab.), "First Searches for Axions and Axionlike Particles with the LUX Experiment", Phys. Rev. Lett. **118**, 261301 (2017).

[17] K. Abe *et al.* (XMASS Collab.), "Search for dark matter in the form of hidden photons and axion-like particles in the XMASS detector", Phys. Lett. B **787**, 153-158 (2018).

[18] M. Agostini *et al.* (GERDA Collab.), "Final Results of GERDA on the Search for Neutrinoless Double-$\beta$ Decay", Phys. Rev. Lett. **125**, 252502 (2020).

[19] M. Agostini *et al.* (GERDA Collab.), "Upgrade for Phase II of the Gerda experiment", Eur. Phys. J. C **78**, 388 (2018).

[20] M. Agostini *et al.* (GERDA Collab.), "Modeling of GERDA Phase II data", J. High Energy Phys. **03**, 139 (2020).

[21] K. H. Ackermann *et al.*, "The GERDA experiment for the search of $0\nu\beta\beta$ decay in $^{76}$Ge", Eur. Phys. J. C **73**, 2330 (2013).

[22] A. Caldwell, D. Kollár, and K. Kröninger, "BAT – The Bayesian analysis toolkit", Comput. Phys. Commun. **180**, 2197–2209 (2009).

[23] M. Agostini *et al.* (GERDA Collab.), "Calibration of the GERDA experiment", Eur. Phys. J. C **81**, 682 (2021).

[24] DDEP data, LNHB [accessed: 2020 June 3]. `http://www.nucleide.org/DDEP_WG/DDEPdata.htm`.

[25] R. Mingazheva and R. Hiller, "Generic peak search and its application to the search for keV-scale Dark Matter", GSTR-19-002 (2019).

[26] XCOM, NIST [accessed: 2020 August 2]. `https://www.nist.gov/pml/xcom-photon-cross-sections-database`.

[27] Y. J. Ko and H. K. Park, "Comments on bosonic super-WIMPs search experiments", arXiv: 2105.11109 (2021).

[28] M. Agostini *et al.* (GERDA Collab.), "Characterization of inverted coaxial $^{76}$Ge detectors in GERDA for future double-$\beta$ decay experiments", Eur. Phys. J. C **81**, 505 (2021).

[29] gerda-metadata, GitHub repository [accessed: 2020 August 26]. `http://github.com/mppmu/gerda-metadata`.